High Resolution NMR Scattering: The First Measurement of Spin Diffusion Rates in a Homogeneous Solid

by

Wurong Zhang

B.S., Engineering Physics, Tsinghua University, Beijing, China (1988)
M.S., Engineering Physics, Tsinghua University, Beijing, China (1991)

Submitted to the Department of Nuclear Engineering
in partial fulfillment of the requirements for the degree of

Doctor of Philosophy in Radiological Sciences

at the

MASSACHUSETTS INSTITUTE OF TECHNOLOGY

FEBRUARY 1998

Author .....
Department of Nuclear Engineering
December 22, 1997

Certified by .....
David G. Cory
Associate Professor of Nuclear Engineering
Thesis Supervisor

Certified by .....
Sow-Hsin Chen
Professor of Nuclear Engineering
Thesis Reader

Accepted by .....
Lawrence M. Lidsky
Chairman, Department Committee on Graduate Students

High Resolution NMR Scattering: The First Measurement of Spin Diffusion Rates in a Homogeneous Solid

by

Wurong Zhang

Submitted to the Department of Nuclear Engineering
on December 22, 1997, in partial fulfillment of the
requirements for the degree of
Doctor of Philosophy in Radiological Sciences

Abstract

The first direct measurement of the rate of spin diffusion through a homogeneous sample was performed as an incoherent NMR scattering experiment. The experiment consists of a combination of pulsed gradient spin echo methods with multiple pulse / pulsed gradient spatial encoding methods. The NMR scattering experiment involves the creation of an initial spatial magnetization grating, a period of spin evolution including the displacement of spin magnetization, followed by the detection of the residual magnetization grating. The essence of NMR scattering measurements is to record the extent of microscopic motion of spin magnetization through a sample by directly observing amplitude and phase changes of a well defined spin magnetization grating. The spin diffusion measurement records the rate of destruction of a magnetization grating by the random offset of spin magnetization associated with the flip-flop term of the homonuclear dipole-dipole interaction.

Since the microscopic motion driven by dipolar coupling is very slow, only fine magnetization gratings are sensitive to the small spatial offsets. Strong pulsed magnetic field gradient techniques were developed for these studies which generate switched gradients with strengths up to $10^3 T/m$ (a factor of 100 stronger than those commercially available, and a factor of 25 stronger than the highest previously reported). These gradients are able to create a spatial magnetization grating with a pitch of from $1\mu m$ to $1nm$ for solid state NMR scattering experiments. Gradients on the order of $200T/m$ were applied in the spin diffusion measurement experiment. For single crystal CaF_2, the measured parallel components of the spin diffusion rates are $7.1 \times 10^{-12} cm^2/s$ along the [0,0,1] direction and $5.3 \times 10^{-12} cm^2/s$ along the [1,1,1] direction, in good agreement with theoretical predictions.

Additional work has been done on flow measurement. A noval approach is introduced to measuring flow velocities using a probe with a spatially varying RF field, and without using other magnetic field gradients. The velocities of the spins are measured as a modulation of the NMR signal from the translation of a spatial magnetization grating through a detection coil with a spatially periodic field profile. Since the same coil can be employed to create the initial magnetization grating, the overall

measurement is as simple as recording the signal modulation frequency following a single excitation pulse. The design principles are discussed for a probe that has a spatially periodic field constructed from a series of lumped element π-circuits. Spatial modulation of the amplitude or the phase of the RF field can easily be achieved, and either of these may be used to characterize a flow field. Examples are shown of measurements of pipe flow using a probe with an amplitude modulated RF field.

Thesis Supervisor: David G. Cory
Title: Associate Professor of Nuclear Engineering

Acknowledgments

I am deeply indebted to my thesis supervisor, Prof. David G. Cory, for his continuous guidance and inspiration during these years at MIT. His profound knowledge in every aspect of magnetic resonance and extraordinary expertise in a varity of experimental techniques and instrumentation have greatly benefited this research. His kindness, enlightenment, and persistent encouragement have made my thesis work a delightful and memorable experience. Throughout these years, David has always been a brilliant mentor as well as a true friend.

My heartfelt thanks also go to my thesis reader, Prof. Sow-Hsin Chen, and go to Prof. Sidney Yip, for their kindness, their constant interest and encouragement in my work, and their invaluable insights and advices.

My sincere gratitude is due to Dr. Werner E. Mass for his always pleasant attitude and friendship, and for many valuable suggestions he has given to my work.

My sincere gratitude is also due to my colleagues for plenty of pleasurable time, fruitful discussions, and warm friendship. Their willingness to assist at any time and their generous help are greatly appreciated.

I'm indebted to my friend Yujie Wang in CMSE of MIT for his patiently helping me with X-ray diffraction techniques to orient and cut CaF_2 single crystals. I'm also very grateful to many friends here at MIT and Boston area for a lot of enjoyable moments which we spent together. My grateful thanks also go to my old friends in China whose friendship has been with me all these years despite we are far away from each other.

I would like to acknowledge the National Science Foundation, the Center for Materials Science and Engineering of MIT, and the National Institutes of Health for their financial support of this research.

My very special thanks go to my wife Fanmin, my parents, my grandparents, my sisters and all my family members for their support, understanding and patience. The emotional tie with them has always been a tremendous motivation for me whenever I am away from my hometown.

This thesis is dedicated to my beloved family.

Contents

List of Figures

List of Tables

Chapter 1

Introduction

Spin diffusion was one of the earliest concepts in NMR of solids having been put forth by Bloembergen in 1949 to account for the unexpectedly rapid spin lattice relaxation found in solids [1]. Since then it has been of considerable theoretical and experimental interest, and yet to date there has been no direct measurement of the spin diffusion rate in a homogeneous solid. This study is the first reported instance of such a measurement.

The exploration of spin diffusion in a single crystal is appealing since the spin Hamiltonian is well known, the initial conditions are well defined, and the dynamics are kinematically simple. The homonuclear dipolar Hamiltonian contains the well-known "flip-flop" term, $I_+I_- + I_-I_+$, which permits energy conserving two-spin flips of anti-parallel aligned spins, and these two spin flips act as a means of transporting spin magnetization through the lattice. In Bloembergen's original analysis the transport is to relaxation sinks created by the fluctuating magnetic fields of paramagnetic impurities. The reduced bulk spin lattice relaxation time is then controlled by the spin diffusion mediated transport of magnetization to the sinks. A clear indication that spin diffusion does indeed govern the bulk relaxation rate is seen from the angular dependence of T_1 in cubic crystals [2, 3]. In the absence of spin diffusion the T_1 of a cubic lattice is isotropic; the observed anisotropies arise from the angular dependence of the dipolar interaction on which the diffusion rate depends.

Since the two spin flip-flop process appears as an elementary step in a random

walk, the long time, large lattice behavior follows a diffusion law, and in the continuum limit, the overall transport of magnetization is Gaussian. For the case of a sinusoidal magnetization grating, Redfield [4] connected the spin diffusion constant to the lineshape moments, and later, Redfield and Yu [5, 6] explicitely worked out the form for spin diffusion constant from moment method. Other groups also investigated this problem using different approaches. Among them, Lowe and Gade [7, 8] derived a diffusion equation from density matrix approach, Borkmans and Walgraef [9] obtained a similiar equation based on irreversible statistical mechanics, and recently, Tang and Waugh [10] computed the diffusion coefficients from classical spin dynamics.

Of course, the short time behavior of the flip-flop process is unitary and a mark of the isolation of the spin system is that even over long times and for processes involving many spins, spin diffusion is reversible, as shown by Waugh and coworkers [11]. In systems that may be described as a small cluster of spins, the unitary behavior is very pronounced [12, 13], and the diffusion analogy is not applicable.

The archetype measurement of spin diffusion involves the creation of a non-uniform magnetization profile throughout the sample and then measuring its rate of returning to spatial uniformity. The experimental challenges are: 1) to create a spatially varying magnetization that has a characteristic length scale shorter than, or on the order of, the root mean square displacement during T_1 ($\Delta z_{rms} = \sqrt{2DT_1}$, where $D \sim 10^{-12} cm^2/s$); and 2) to create this profile over an area that has a uniform spin Hamiltonian. Prior to this study, there has been no successful measurement of spin diffusion rates in a homogeneous solid.

In this work, the measurement of spin diffusion was performed as an incoherent NMR scattering experiment. The essence of NMR scattering measurements is to record the extent of microscopic transport of spin magnetization through a sample by directly observing amplitude and phase changes of a well defined spin magnetization grating. As is well known from coherent approaches to magnetic resonance imaging, the linear increasing rate of spin precession in a magnetic field gradient creates a spatial grating of the transverse nuclear spin magnetization. The grating

is a spatially periodic modulation of the phase of the magnetization since over time each precessing spin picks up a phase factor of $e^{-i\gamma\frac{\partial B_z}{\partial z}zt}$, where γ is the gyromagnetic ratio, and $\frac{\partial B_z}{\partial z}$ is the gradient strength. This grating is a linear ramp of the transverse magnetization's relative phase and the spatial period defines a wavenumber, k, that in the simplest case is proportional to the first moment of the gradient waveform. In an NMR scattering experiment, such a magnetization grating is created, followed by an interval of magnetization translation, and then the resultant changes in the grating are recorded. To date, NMR scattering measurements have relied on molecular diffusion to carry the spin magnetization through the sample. The new measurement is the first instance of a scattering measurement in a well defined sample where spin diffusion is responsible for the transport of the magnetization. Fischer, Kimmich and Fatkulin [14] have recently observed a contribution to magnetization diffusion in polymer melts that is attributed to spin diffusion.

In the case of a solid sample with strong homonuclear dipolar couplings, the measurement must be carried out in such a fashion as to account for both the short spin-spin relaxation time, and to suspend spin diffusion during the preparation of the magnetization grating. A similar requirement is encountered in solid state imaging [15] where a combination of multiple pulse coherent averaging interspersed with pulsed magnetic field gradients [16] has been employed to interrupt the dipolar evolution during the creation of magnetization gratings. In this experiment a magic echo sequence [11, 17, 18] is used to periodically refocus the evolution from dipolar coupling and since spin diffusion is also driven by dipolar coupling there is no net spin diffusion during the creation of the grating. The experimental ability to suppress spin diffusion during the creation of the grating makes the analysis of the diffusion data very simple and is analogous to being in the "delta gradient pulse" limit for pulsed gradient diffusion measurements in liquids.

The effectiveness of using a magic echo sequence to lengthen the decay of the transverse magnetization depends both on the sample purity and on the experimental conditions. The instrumentational factors, such as RF phase transients, finite RF field strengths, and the impurities of RF frequencies, are unavoidable and affect the

performance of the pulse sequence. In practice, there is a limited time during which to apply magnetic field gradient. To create a magnetization grating with a pitch of from $1\mu m$ to $1nm$ for solid state NMR scattering studies, pulsed gradients on the order of $10^2 T/m$ to $10^3 T/m$ are necessary.

Strong pulsed magnetic field gradient techniques were developed for these studies which generate switched gradients with strengths up to $10^3 T/m$ (a factor of 100 stronger than those commercially available, and a factor of 25 stronger than the highest previously reported). Meanwhile, small sample sizes, large pulsed currents, coil heating, strong Lorentz forces and torques dramatically increased the difficulties of the experiment.

The order of this thesis is the following: Chapter 1 is the introduction; Chapter 2 reviews spin diffusion theories and previous experiments; Chapter 3 describes the proposed new approach of spin diffusion measurement by NMR incoherent scattering method; Chapter 4 covers strong pulsed magnetic field gradient probe design; Chapter 5 describes a home-built NMR spectrometer, provides the detailed pulse sequence for spin diffusion measurement, and provides and discusses the experimental results; Chapter 6 is the conclusion and also discusses future studies of high resolution NMR scattering. Chapter 7 is an independent chapter of additional work which describes a noval approach of measuring flow velocities via spatially varying RF fields and provides a unique way of designing amplitude modulated and phase modulated NMR probes.

Chapter 2

Review of Spin Diffusion: Theories and Experiments

2.1 Review of Spin Diffusion Theories

2.1.1 Dipole-Dipole Interaction

Spin diffusion was first invoked by Bloembergen [1] in 1949 to account for the unexpectedly rapid spin lattice relaxation found in solids. To understand this concept, it is necessary to briefly review the dipole-dipole interaction, which describes the coupling between two nearby magnetic moments. In the quantum mechanical treatment, the two-spin dipole-dipole interaction Hamiltonian is written as,

$$\mathbf{H}_d = \frac{\gamma_1\gamma_2\hbar^2}{r^3}\left\{\mathbf{I}_1\cdot\mathbf{I}_2 - 3\frac{(\mathbf{I}_1\cdot\mathbf{r})(\mathbf{I}_2\cdot\mathbf{r})}{r^2}\right\}, \tag{2.1}$$

where γ_1 and γ_2 are the gyromagnetic ratios of two nuclei with angular momentum $\mathbf{I}_1$ and $\mathbf{I}_2$ respectively, and $\mathbf{r}$ is a position vector connecting them. By decomposing $\mathbf{I}_1$, $\mathbf{I}_2$ and $\mathbf{r}$ into their x, y, z components, realizing that $I_x = (I_+ + I_-)/2$, $I_y = (I_+ - I_-)/2i$, $x/r = \sin\theta\cos\phi$, $y/r = \sin\theta\sin\phi$, $z/r = \cos\theta$, and summing over all spins, the dipolar interaction Hamiltonian for the entire spin system can be written in a more

meaningful form,

$$\mathbf{H}_d = \sum_{i>j} \frac{\gamma_i \gamma_j \hbar^2}{r_{ij}^3}(A + B + C + D + E + F), \tag{2.2}$$

where

$$A = I_{iz} I_{jz}(1 - 3\cos^2\theta_{ij}), \tag{2.3}$$

$$B = -\frac{1}{4}(I_{i+} I_{j-} + I_{i-} I_{j+})(1 - 3\cos^2\theta_{ij}), \tag{2.4}$$

$$C = -\frac{3}{4}(I_{i+} I_{jz} + I_{iz} I_{j+}) \sin 2\theta_{ij} e^{-i\phi_{ij}}, \tag{2.5}$$

$$D = -\frac{3}{4}(I_{i-} I_{jz} + I_{iz} I_{j-}) \sin 2\theta_{ij} e^{i\phi_{ij}}, \tag{2.6}$$

$$E = -\frac{3}{4} I_{i+} I_{j+} \sin^2\theta_{ij} e^{-2i\phi_{ij}}, \tag{2.7}$$

$$F = -\frac{3}{4} I_{i-} I_{j-} \sin^2\theta_{ij} e^{2i\phi_{ij}}. \tag{2.8}$$

The physical meaning of these terms can be understood through state transitions. Among them, term A causes no transition, term C flips one spin up and term D flips one spin down, similiarly, term E flips two spins up and term F flips two spins down. Of all the six terms, the one of most interest here is term B, which simultaneously flips one spin up and another spin down. If the two nuclei are identical, this flip-flop process is energy conserving. Given an initially non-uniform spatial distribution of spin polarization in an otherwise homogeneous system, the flip-flop term will drive a diffusive process which will return the system to a spatially uniform spin magnetization. In the long time large distance regime, this process follows a diffusion equation and is referred as *Spin Diffusion*. In the spin diffusion case, only spin coherence is transfered, and the spin itself remains physically fixed. In the next few subsections, various theories and methods to derive the spin diffusion equation and to calculate the spin diffusion coefficients are reviewed.

2.1.2 Bloembergen's Original Analysis of Spin Diffusion

In experiments with ionic crystals (diamagnetic insulators), such as CaF_2, Bloembergen [1] found that the measured spin lattice relaxation times are several orders faster than that expected from conventional theory of relaxation where time variations in local fields caused by lattice vibrations were regarded as the major relaxation mechanism. To resolve this discrepancy, Bloembergen suggested that paramagnetic impurities present in these crystals play a predominant role in the relaxation process, since each paramagnetic impurity generates fluctuating magnetic fields which provide a wide energy spectrum, the spins nearby are efficiently relaxed. The concentration of paramagnetic impurities is however dilute, and most nuclear spins are far from the "relaxation center". Bloembergen then suggested that the energy conserving "flip-flop" process, driven by term B of the dipolar interaction Hamiltonian, serves as a mechanism to transfer the polarizations of remote spins to those spins near paramagnetic impurities. The following simple argument, which basically followed Bloembergen's original derivation, but was made clearer in Abragam's treatise [19], shows why this process follows a diffusion equation.

We will consider a simple cubic lattice of spin $\frac{1}{2}$ nuclei, with nearest spin distance a and limit the dynamics to mutual flips between only nearest neighbor spins. With p_+ and p_- giving the probabilities of spin up and spin down and W the probability of a transition, then, the dynamics are governed by the coupled differential equation,

$$\frac{\partial p_+(x)}{\partial t} = W\Big\{p_-(x)[p_+(x+a)+p_+(x-a)] - p_+(x)[p_-(x+a)+p_-(x-a)]\Big\}, \quad (2.9)$$

and,

$$\frac{\partial p_-(x)}{\partial t} = W\Big\{p_+(x)[p_-(x+a)+p_-(x-a)] - p_-(x)[p_+(x+a)+p_+(x-a)]\Big\}. \quad (2.10)$$

These may be rewritten in terms of the spin polarization ($p = p_+ - p_-$) as,

$$\frac{\partial p(x)}{\partial t} = 2W\Big\{p_-(x)[p_+(x+a)+p_+(x-a)] - p_+(x)[p_-(x+a)+p_-(x-a)]\Big\}. \quad (2.11)$$

Since $p_+ + p_- = 1$, and $p_+ = (1+p)/2$, $p_- = (1-p)/2$, then,

$$\frac{\partial p(x)}{\partial t} = W[p(x+a) + p(x-a) - 2p(x)]. \tag{2.12}$$

It has been argued that it is reasonable to assume that $p(x)$ varies slowly at the length scales of a (a few $\mathring{A}$), so that (2.12) can be approximated by a diffusion equation:

$$\frac{\partial p}{\partial t} = Wa^2 \frac{\partial^2 p}{\partial x^2}, \tag{2.13}$$

where the diffusion constant is given by,

$$D = Wa^2 \approx \frac{a^2}{50T_2}. \tag{2.14}$$

For single crystal CaF_2, $a \approx 2.7 \times 10^{-8} cm$, $T_2 \approx 10^{-5} s$, the diffusion constant was estimated to be on the order of $10^{-12} cm^2/s$.

Such an analysis can be extended to a three dimensional form, however, in doing so, caution must be exercised since the anisotropies of W result in a diffusion tensor, not an isotropic diffusion constant.

2.1.3 Redfield and Yu's Calculation of Diffusion Coefficients from the Moment Method

In 1959, Redfield [4] outlined a procedure to evaluate the spin diffusion coefficients from moment calculation, and later, Redfield and Yu [5, 6] demonstrated explicitly their moment method. They argued that the decay of a spatially sinusoidally varying magnetization can not be exponential at the very beginning since the first derivative of the decay function should initially be zero. However, after a short time T_j ($T_j << \tau$, where τ is the decay constant), the decay can be exponential. Thus, the Fourier transform of this decay function should be nearly Lorentzian, except for $\omega > T_j^{-1}$. Following this argument, they guessed a form of the Fourier transform of the decay

function,

$$A(\omega) = \frac{2\tau/\pi}{1+\omega^2\tau^2} g(\omega), \tag{2.15}$$

where $g(\omega)$ was introduced to cut off the Lorentzian for $\omega > T_j^{-1}$.

Since $\omega^2 A(\omega) \approx (2/\pi\tau)g(\omega)$ for $\omega > \tau^{-1}$, the second moment becomes,

$$M_2 \approx \frac{2}{\pi\tau}\int_0^\infty g(\omega)d\omega, \tag{2.16}$$

and likewise,

$$\frac{M_4}{M_2} \approx \frac{\int_0^\infty \omega^2 g(\omega)d\omega}{\int_0^\infty g(\omega)d\omega}. \tag{2.17}$$

Since $\tau^{-1} = Dk^2$, where k is the wavenumber of a spatially sinusoidally varying magnetization, and D is the diffusion coefficient, by assuming $g(\omega)$ is Gaussian, they obtained,

$$D = (M_2/k^2)(\pi M_2/2M_4)^{1/2}. \tag{2.18}$$

Thus, they reduced the problem of analyzing the temporal decay of a spatially sinusoidally varying magnetization to a moment calculation.

Following Van Vleck's moment expressions [20], the $2n$th moment can be calculated as,

$$M_{2n} = \frac{\sum_{\alpha\beta}(\omega_\alpha - \omega_\beta)^{2n} \mid P_{\alpha\beta} \mid^2}{\sum_{\alpha\beta} \mid P_{\alpha\beta} \mid^2}, \tag{2.19}$$

where $P_{\alpha\beta}$ is the matrix component of a time-dependent perturbation, and $\mid P_{\alpha\beta} \mid^2$ is proportional to the transition rate between states α and β.

By writing the perturbation Hamiltonian as,

$$P(t) = \epsilon \sum_i cos(\omega t) sin(kx_i) S_{iz}, \tag{2.20}$$

where the summation is over all spins in x direction, and writing the truncated Hamiltonian as

$$H = \frac{1}{2}\sum_{kl}(A_{kl}S_{k+}S_{l-} + B_{kl}S_{kz}S_{lz}) + \sum_k \hbar\gamma H_0 S_{kz}, \tag{2.21}$$

they worked out an explicit form for the diffusion coefficients of Zeeman energy,

D_z, which is the diffusion coefficient of the magnetization. For lattices with pure dipole-dipole interaction, they further simplified the calculation by assuming that $B_{kl} >> A_{kl}$ and thus ignored higher order A_{kl} terms. Finally they simplified the lattice summation, while introducing some errors, by allowing the sum over identical spins. The final estimate they obatined for the diffusion coeffcient of Zeeman energy in a lattice with dipolar coupling is,

$$D_z \approx \frac{\pi^{1/2} S(S+1) \sum_j x_{ij}^2 A_{ij}^2}{4\hbar^2 < \Delta\omega^2 >^{1/2}}, \tag{2.22}$$

where $< \Delta\omega^2 >$ is the Van Vleck second moment of the resonance lineshape.

It is noted that the assumption of $B_{kl} >> A_{kl}$ is not strictly true in the dipole-dipole case. As shown in (2.3) and (2.4), B_{kl} in (2.21) is only twice as large as A_{kl}.

2.1.4 Tang and Waugh's Calculation of Spin Diffusion Coefficients from Classical Spin Dynamics

In addition to the original analysis by Bloembergen and the moment method by Redfield and Yu, there are three other calculations of particular note. Lowe and Gade [7, 8] derived the spin diffusion equation using a density matrix approach, and evaluated the average diffusion coefficients for a simple cubic lattice with the external field along the [100], [110], and [1,1,1] axes. Borkmans and Walgraef [9] derived the diffusion equation from irreversible statistical mechanics, and explicitly calculated the $D_{||}$, $D_{\perp}$, and D_{eff} with the external field along the [100], [110], and [111] axes of single crystal CaF_2, where $D_{||}$, $D_{\perp}$ are the components of spin diffusion coefficients for diffusion parallel or perpendicular to the external field, and D_{eff} is the average diffusion coefficient. Apart from above methods, Morita [21] used a "memory function" method analyzing the spin diffusion in Heisenberg magnets.

Recently, Tang and Waugh [10] chose to investigate this subject from a classical approach. They considered each spin j in a lattice as a classical gyromagnet, with a magnetic momentum $\mathbf{m}_j$ which experiences a local field $\mathbf{B}_j$ arising from all its

neighbors,

$$\mathbf{B}_j = \sum_{k \neq j} \mathbf{B}_j^k. \tag{2.23}$$

The truncated dipolar field from like spins is

$$\mathbf{B}_j^k = -\frac{1 - 3\cos^2\theta_{jk}}{2r_{jk}^3}(m_{Xk}\mathbf{i} + m_{Yk}\mathbf{j} - 2m_{Zk}\mathbf{k}). \tag{2.24}$$

By specifying the initial condition of a sinusoidally varying magnetization, and using the classical equation

$$\frac{d\mathbf{m}_j}{dt} = \gamma \mathbf{m}_j \times \mathbf{B}_j, \tag{2.25}$$

they were able to follow the evolution of the spatially varying magnetization via computer simulations. Their simulation showed that the process did follow a diffusion course, and the diffusion coefficients of both the Zeeman energy and the spin-spin energy were calculated for a single crystal CaF_2 at various crystal orientations. All of their results yield the same order of magnitude in the classical many spin limit.

2.2 Previous Spin Diffusion Measurements

The archetype measurement of spin diffusion involves the creation of a non-uniform magnetization profile throughout the sample and then measuring its rate of returning to spatial uniformity. So far, nearly all approaches to creating a spatially varying magnetization profile have involved the use of chemically heterogeneous samples, either based on the morphology of semicrystalline polymers [22], diffusion in melts [14], diffusion in blends [23, 24], or exploring small spin systems [25]. While these measurements are useful to characterize the morphology of the sample, most have little relationship to theoretical studies since the spectral difference that permitted the creation of the magnetization profile complicates the analysis by introducing a spin-diffusion bottle neck where the flip-flop term is no longer energy conserving.

single crystal CaF_2, in which the ^{19}F nuclei have spin $\frac{1}{2}$ and compose a simple cubic lattice, is the one of most interest in rigid solid spin diffusion studies because

of its simple structure and pure dipole-dipole interactions. However, the extremely slow diffusion rates (predicted to be on the order of $10^{-12}cm^2/s$ or $10^{-13}cm^2/s$) have brought tremendous difficulties for a quantitative measurement. Researchers had to attack the problem indirectly by studying the spin lattice relaxation in crystals with paramagnetic impurities. It was shown by Blumberg [26] that, when impurities are far apart from each other, which is the diffusion limited relaxation case, for times very short compared to T_1, the relaxation due to interactions with impurities dominates and the magnetization recovery after saturation has a $t^{1/2}$ behavior whose factor can be subtracted and be related to the diffusion coefficients. Later, Leppelmeier and Jeener [3] made a measurement of the diffusion coefficients in CaF_2 doped with U^{3+} based on this theory. Their measurements of the effective diffusion coefficient with the external field along [100] direction agreed with theoretical predictions, but that with the external field along [111] direction was an order magnitude smaller than theoretical predictions.

This approach, which relied upon paramagnetic impurities, is however complicated by the "diffusion barriers" which exist immediately surrounding the impurities. The energy mismatch in this area prohibited energy conserving mutual spin flips. In addition, the $t^{1/2}$ behavior only provides a factor which is indirectly related to the diffusion coefficients, and the $t^{1/2}$ domain is so small that it is barely distinguishable from the t behavior. Therefore the accuracy of this method is quite limited.

Kuhns, Hammel, Gonen and Waugh [27] attempted to carry out a direct measurement of spin diffusion in CaF_2 through a series of low temperature experiments of relaxation in a single crystal whose surface was efficiently relaxed through contact with a ^{3}He bath. The experiment was designed to measure the return to thermal equilibrium of a sample that was initially saturated, with special attention paid to the long time behavior so that surface effects would not be important. Unfortunately, the bulk ^{19}F relaxation time was unexpectedly fast preventing the long time scale necessary for the measurement.

Prior to the results presented here, there has been no direct measurement of the spin diffusion rates in a homogeneous solid.

Chapter 3

Proposed Measurement of Spin Diffusion Rates in a Homogeneous Solid via NMR Incoherent Scattering Experiment

In this study, it is chosen to approach a measurement of spin diffusion as an incoherent NMR scattering experiment. To describe this, it is necessary to introduce the concept of magnetization grating, which plays a central role in NMR scattering experiments.

3.1 The Concept of Magnetization Grating

A *magnetization grating* is a spatially periodic modulation of the amplitude or phase of the magnetization in a sample. This is generally achieved by the application of RF pulses and magnetic field gradients.

In a typical NMR experiment, the sample is subjected to a strong external magnetic field $\mathbf{B} = B_0\hat{z}$, and, at equillibrium, a nuclear magnetization is induced,

$$\mathbf{M} = \chi_0\mathbf{B}, \tag{3.1}$$

where χ_0 is the static nuclear susceptibility of the sample.

A 90^0 RF pulse nutates the equilibrium magnetization into a plane perpendicular to the z-axis (which is thus called the transverse plane), then the magnetization in the transverse plane will precess around the z-axis according to,

$$\frac{d\mathbf{M}}{dt} = \gamma \mathbf{M} \times \mathbf{B}, \tag{3.2}$$

where γ is the gyromagnetic ratio of the nuclei. The angular frequency of this precession is characterized by,

$$\omega_0 = -\gamma B_0. \tag{3.3}$$

In the presence of a magnetic field gradient,

$$\mathbf{G} = \frac{\partial B_z}{\partial x}\hat{x} + \frac{\partial B_z}{\partial y}\hat{y} + \frac{\partial B_z}{\partial z}\hat{z}, \tag{3.4}$$

the precession frequency is modified as,

$$\omega_0(\mathbf{r}) = -\gamma(B_0 + \mathbf{G} \cdot \mathbf{r}). \tag{3.5}$$

For a pulsed gradient time period, δ, the transverse magnetization gains a linear phase ramp from the gradient evolution, $e^{-i\mathbf{k}\cdot\mathbf{r}}$, where $\mathbf{k} = \gamma\mathbf{G}\delta$. The spatially modulated magnetization is then called a magnetization grating, and $\mathbf{k}$ is the wavevector of the grating.

3.2 The Creation of a Magnetization Grating in Rigid Solids

A magnetization grating can easily be created in liquids by simply applying a magnetic field gradient when the magnetization is in the transverse plane. Since the dipolar interactions are averaged out due to the physical motions of spins, the resonance lines are sharp and the spin-spin relaxation times (T_2) are sufficiently long to allow fine

gratings to be prepared.

In rigid solids, however, the dipolar interaction dominates the spin-spin relaxation process. T_2 for these materials are very short, for instance, for single crystal CaF_2, T_2 is on the order of $10\mu s$. The transverse magnetization will thus lose its phase coherence very quickly.

A varity of techniques have been developed to overcome the strong dipole-dipole interactions in solids, usually by performing coherent averaging either in the spin space or in the coordinate space.

Since the creation of a necessarily fine magnetization grating is a prerequisite for solid state NMR scattering experiments, and coherent averaging techniques are indispensable for the creation of such a grating, it is worthwhile to discuss one such technique in detail. A magnetization grating can be created by combining coherent averaging with gradient pulses.

Rhim, Pines and Waugh [11] developed the magic echo sequence which, ideally, can completely refocus the spin evolution due to dipole-dipole interactions. Basically, this is achieved by realizing that, under a strong RF irradiation, the dipolar interaction Hamiltonian gains a negative sign. To show this, consider the Hamiltonian of a spin system under a strong RF irradiation,

$$\mathbf{H} = \mathbf{H}_0 + \mathbf{H}_1 + \mathbf{H}_d, \tag{3.6}$$

where

$$\mathbf{H}_0 = -\gamma\hbar B_0 \sum_i I_{iz} = \hbar\omega_0 I_z, \tag{3.7}$$

is the Zeeman Hamiltonian with $I_z = \sum_i I_{iz}$ and $\omega_0 = -\gamma B_0$, and,

$$\mathbf{H}_1 = -2\gamma\hbar B_1 \cos(\omega t) \sum_i I_{ix} = 2\hbar\omega_1 \cos(\omega t) I_x, \tag{3.8}$$

is the Hamiltonian due to the RF irradiation with $I_x = \sum_i I_{ix}$ and $\omega_1 = -\gamma B_1$, and $\mathbf{H}_d$ is the dipolar interaction Hamiltonian expressed as (2.2).

The evolution of the spin system is subjected to the Schrödinger equation,

$$i\hbar\frac{d\psi}{dt} = \mathbf{H}\psi. \tag{3.9}$$

By transforming to a frame rotating around the z-axis with an angular frequency ω (which is thus called the rotating frame), that is, by performing,

$$\psi = U_R\psi_R, \tag{3.10}$$

where

$$U_R = e^{-i\omega t I_z}, \tag{3.11}$$

then,

$$i\hbar\frac{d\psi_R}{dt} = \mathbf{H}_R\psi_R, \tag{3.12}$$

where

$$\mathbf{H}_R = \{U_R^{-1}\mathbf{H}U_R - i\hbar U_R^{-1}\frac{dU_R}{dt}\}. \tag{3.13}$$

All terms containing $e^{\pm i\omega t}$ or $e^{\pm i2\omega t}$ introduce fast oscillations. In NMR experiments, the RF frequency is on the order of a few hundred MHz, and the detected NMR signal in the rotating frame is at the audio frequency range (kHz). Therefore, the effect of the fast oscillations will be averaged out, and it is justified to write a truncated Hamiltonian as,

$$\mathbf{H}_R = \mathbf{H}_e^R + \mathbf{H}_d^0, \tag{3.14}$$

where

$$\mathbf{H}_e^R = \hbar(\omega_0 - \omega)I_z + \hbar\omega_1 I_x, \tag{3.15}$$

is the Hamiltonian due to the effective field, and,

$$\mathbf{H}_d^0 = \sum_{i>j}\frac{\gamma^2\hbar^2}{r_{ij}^3}\frac{(1-3\cos^2\theta_{ij})}{2}(3I_{iz}I_{jz} - \mathbf{I}_i\cdot\mathbf{I}_j), \tag{3.16}$$

is the truncated dipolar interaction Hamiltonian.

A second coordinate transformation can be done so that the effective field is along

the z-axis of the new coordinate (called the tilted rotating frame). This is achieved by a unitary transformation,

$$\psi_R = U_T \psi_{TR}, \tag{3.17}$$

where

$$U_T = e^{i\beta I_y}, \tag{3.18}$$

with

$$\beta = \cos^{-1} \frac{\omega_0 - \omega}{\omega_e}, \tag{3.19}$$

and

$$\omega_e = \sqrt{(\omega_0 - \omega)^2 + \omega_1^2}. \tag{3.20}$$

(3.12) then becomes,

$$i\hbar \frac{d\psi_{TR}}{dt} = \mathbf{H}_{TR} \psi_{TR}. \tag{3.21}$$

Since U_T is not a function of time, $\mathbf{H}_{TR}$ is expressed as,

$$\mathbf{H}_{TR} = U_T^{-1} \mathbf{H}_R U_T. \tag{3.22}$$

When the effective field is much larger than the dipolar coupling strength, the dipolar interaction Hamiltonian will be truncated again in the tilted rotating frame, and it is easy to show,

$$\mathbf{H}_{TR} = \hbar \omega_e I_z + \frac{(3\cos^2\beta - 1)}{2} \mathbf{H}_d^0, \tag{3.23}$$

where $\mathbf{H}_d^0$ is the truncated dipolar Hamiltonian in the rotating frame expressed by (3.16).

Thus, the dipole-dipole interaction Hamiltonian has obtained an additional factor $(3\cos^2\beta - 1)/2$ due to the strong RF irradiation. When $cos^{-1}(1/\sqrt{3}) < \beta < \pi - cos^{-1}(1/\sqrt{3})$, this factor is negative. By designing an appropriate pulse sequence, the evolution due to the dipolar interaction can be reversed, and an echo called magic echo is obtained. This technique is therefore referred as a time reversal technique by

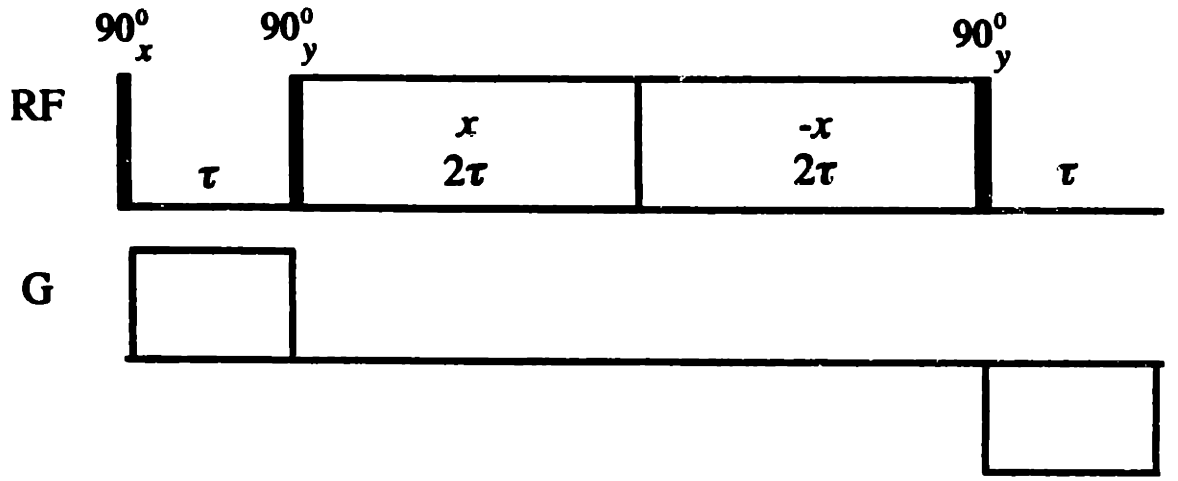

Figure 3-1: A magic echo sequence with pulsed magnetic field gradients added to create a spatial spin magnetization grating in rigid solids, The first 90^0_y pulse performs the coordinate transformation from the rotating frame into the tilted rotating frame. The second 90^0_y pulse can be taken as the combination of a 90^0_{-y} pulse and a 180^0_y pulse, where the 90^0_{-y} pulse performs the coordinate transformation from the tilted rotating frame back into the rotating frame, and the 180^0_y pulse refocuses any evolution due to chemical shifts, static field inhomogeneities and susceptibilities. The evolution due to gradient pulses is kept since the sign of the second gradient pulse is intentionally inverted. The phases of the RF irradiations are also alternated for the same period of time to cancel out any RF field inhomogeneity.

Rhim, Pines and Waugh [11].

It is straightforward to combine this technique with pulsed gradients to create a magnetization grating in rigid solids. An example of this is shown in Figure 3-1, where β is chosen to be $\pi/2$ (for on-resonance irradiation), so that $(3\cos^2\beta - 1)/2 = -1/2$, and a RF irradiation period twice as long as that without RF irradiation is used to exactly refocus the dipolar evolution. By alternating the phases of RF irradiation and incorporating an effective 180^0_y pulse (explained in the figure caption), the pulse sequence shown in Figure 3-1 has the added advantages of avoiding RF inhomogeneities and refocusing evolutions due to chemical shifts, static field inhomogeneities and susceptibilities.

A train of magic echo sequences with pulsed gradients can be applied to create a fine magnetization grating in solids. However, the effectiveness of using a magic echo

train to lengthen the decay of the transverse magnetization depends both on the sample purity and on the experimental conditions. The instrumentational factors, such as RF phase transients, finite RF field strengths, and the impurities of RF frequencies, are unavoidable and affect the performance of the pulse sequence. In practice, there is a limited time during which to apply magnetic field gradient. Generally, to create a magnetization grating with a pitch of from $1\mu m$ to $1nm$ for solid state NMR scattering studies, pulsed gradients on the order of $10^2 T/m$ to $10^3 T/m$ are necessary. The design of strong pulsed magnetic field gradient probes will be covered in the next chapter.

3.3 NMR Incoherent Scattering Measurement of Spin Diffusion Rates in a Homogeneous Solid

The NMR scattering experiment involves the creation of an initial spatial magnetization grating, a period of spin evolution including the displacement of spin magnetization, followed by the detection of the residual magnetization grating. The essence of NMR scattering measurements is to record the extent of microscopic motion of spin magnetization through a sample by directly observing amplitude and phase changes of a well defined spin magnetization grating.

Consider the spin density distribution and the linear phase ramp created by the application of a magnetic field gradient, the magnetization is,

$$\mathbf{M}(\mathbf{r}) = \rho(\mathbf{r}) e^{-i\mathbf{k}\cdot\mathbf{r}}, \tag{3.24}$$

where $\rho(\mathbf{r})$ is the spin density.

The displacement of the spin magnetization may be described by a displacement probability $P(\Delta\mathbf{r}, t)$, so that the final magnetization is the convolution of the original magnetization with $P(\Delta\mathbf{r}, t)$,

$$\mathbf{M}(\mathbf{r}, t) = [\rho(\mathbf{r}) e^{-i\mathbf{k}\cdot\mathbf{r}}] \otimes P(\mathbf{r}, t). \tag{3.25}$$

Since the NMR signal is the integral of the spin magnetization over the entire sample volume, to measure the amplitude and phase of the **k**-component of the residual magnetization grating, a second interval of spin precession in the magnetic field gradient is required to unwind the phase ramp, and the resultant signal is,

$$\begin{aligned} S(t) &= \int \{[\rho(\mathbf{r})e^{-i\mathbf{k}\cdot\mathbf{r}}] \otimes P(\mathbf{r},t)\}e^{i\mathbf{k}\cdot\mathbf{r}}d\mathbf{r} \\ &= \tilde{\rho}(0)\tilde{P}(\mathbf{k},t), \end{aligned} \tag{3.26}$$

where $\tilde{\rho}(0)$ is the zero-frequency component of the Fourier transform of the spin density $\rho(\mathbf{r})$, which is equivalent to the integral of spin density over the entire sample volume, and $\tilde{P}(\mathbf{k},t)$ is the **k**-component of the Fourier transform of the displacement probability.

From (3.26), it is seen that the NMR scattering signal is a direct measurement of a selected Fourier component of the displacement probability. Since the signal is derived from all spins in the sample, the S/N of the scattering measurement is not related to the resolution.

To date, NMR scattering measurements have relied on molecular diffusion to carry the spin magnetization through the sample. The new measurement is the first instance of a scattering measurement in a well defined sample where spin diffusion is responsible for the transport of the magnetization.

The spin diffusion measurement records the rate of destruction of a magnetization grating by the random offset of spin magnetization associated with the flip-flop term of the homonuclear dipole-dipole interaction. Here, consider a one-dimensional M_z grating along the z-axis, with a form of,

$$M_z(z) = \rho(z)\cos(kz), \tag{3.27}$$

where k is the wavenumber of the grating.

In the long time/many spin limit of spin diffusion, a Gaussian displacement prob-

ability is expected,

$$P(z,t) = \frac{1}{\sqrt{4\pi D_{||} t}} e^{-z^2/4D_{||}t}, \tag{3.28}$$

where $D_{||}$ is the component of spin diffusion coefficient parallel to the z-axis, which is the direction of the external magnetic field. Therefore the magnetization grating is blurred by the random motion of the spin magnetization,

$$M_z(z,t) = [\rho(z)\cos(kz)] \otimes P(z,t), \tag{3.29}$$

and the resultant signal is,

$$\begin{aligned} S(t) &= \int \{[\rho(z)\cos(kz)] \otimes P(z,t)\} e^{ikz} dz \\ &= \frac{1}{2}[\tilde{\rho}(0) + \tilde{\rho}(2k)] e^{-k^2 D_{||} t}. \end{aligned} \tag{3.30}$$

Since the grating wavenumber k is several orders magnitude larger than the sample bandwidth, $\tilde{\rho}(2k) \approx 0$, the signal is still only a function of $e^{-k^2 D_{||} t}$, the k-component of the Fourier transform of the displacement probability, which provides a direct measurement of the parallel component of the spin diffusion coefficient, $D_{||}$.

Chapter 4

Strong Pulsed Magnetic Field Gradient NMR Probe Design

4.1 Background

Magnetic field gradients are widely employed in NMR [28] for imaging, diffusion studies, coherent pathway selection, solvent suppression, and with sufficiently strong gradients they can be used to explore the structure and dynamics of dipolarly coupled spins via high resolution NMR scattering experiments.

Large static magnetic field gradients are well known in NMR experiments with the gradients originating either from the fringe fields of large magnets or from the magnetic properties of the sample itself. Genack and Redfield [29, 30] studied the dipolar energy dissipation and nuclear spin diffusion under static gradients of more than $10^5 T/m$ by looking near the surface of a type II superconductor. Samoilenko et al [31] used the stray field of $30T/m$ near the end of a superconducting solenoid for subsurface imaging of solids. Kimmich et al [32] used the fringe fields of $10T/m$ and $42T/m$ of superconducting magnets for measuring small self-diffusion coefficients, including studies [14] with fringe fields of 32T/m and 60T/m where spin diffusion was observed in melts of entangled polymers. Using force detection, Züger et al [33] recorded three-dimensional images of an ammonium nitrate sample with a gradient of $2200T/m$ generated by a small nearby magnetic particle, and Schaff and Veeman [34]

have also used force detection with a gradient of $500T/m$ generated with a somewhat larger magnetic particle. While static gradients have the advantages of high strength, excellent stability and no heating, they are difficult to combine with multiple pulse coherent averaging, since the offset dependence of such methods complicates the creation of a spatially uniform grating. For these applications, pulsed gradients have an advantage since it is known how to combine them with multiple pulse cycles while avoiding offset variations [16, 18, 35]. Unfortunately, pulsed gradients are generally much weaker than static gradients.

Pulsed magnetic field gradients are routinely used in spatial NMR experiments and various designs are well known, including Stejskal and Tanner's design of a pulsed Maxwell pair at $1T/m$ for diffusion studies [36, 37], Karlicek and Lowe's quadrupole gradient set of $16T/m$ for diffusion measurements in samples with small diffusion coefficients [38]. For microscopy studies, pulsed gradients on the order of $10T/m$ are widely used [28, 39]. For solid state scattering experiments, however, much stronger gradients are required.

The essence of NMR scattering is to record the extent or variance of microscopic displacement of spin coherence by directly observing the amplitude and phase changes of a well defined spin magnetization grating. In solid state scattering experiments, the spin magnetization displacement is driven by the dipole-dipole interaction. The process is very slow, and in the case of a ^{1}H or ^{19}F rich rigid solid, the spin diffusion coefficient, D, is of order $10^{-4}\mu m^2/s$ or $10^{-5}\mu m^2/s$. To be able to detect these small spatial offsets, the characteristic length scale of the magnetization grating has to be shorter than, or on the order of, the root mean square displacement during the spin lattice relaxation time ($\Delta z_{rms} = \sqrt{2DT_1}$). The pitch of a magnetization grating is inversely proportional to the first moment of the gradient waveform. With a gradient of $100T/m$, a total time of $\sim 25ms$ is needed to create a magnetization grating with a pitch of $10nm$. The gradient pulse width, however, is limited in solid state NMR experiments by the size of windows in multiple pulse cycles. Generally, to create a magnetization grating with a pitch of from $1\mu m$ to $1nm$ for solid state NMR scattering studies, pulsed gradients on the order of $10^2T/m$ to $10^3T/m$ are necessary.

4.2 Gradient Coil Design

Typically $\partial B_z/\partial z$ gradient coils have one of two symmetries, a Maxwell pair [37], or a quadrupole [38], and the general features have been described by Suits and Wilken [40]. For the designs used here the Maxwell pair geometry is prefered since it is easier to construct at very small dimensions, and good gradient profiles are obtained with very few turns.

A Maxwell pair consists of a set of circular loops with currents of equal amplitudes but opposite directions, and it generates magnetic field gradients symmetric about the mid-plane and about the central axis. To derive a convenient formula to calculating this, it is necessary to start from the Biot-Savart Law, which says,

$$\mathbf{B}(\mathbf{r}) = \frac{\mu}{4\pi}\oint_C \frac{I d\mathbf{s} \times \mathbf{R}}{R^3}, \tag{4.1}$$

where $\mathbf{B}(\mathbf{r})$ is the magnetic field at $\mathbf{r}$. The integration path is over a closed current path C, with $Id\mathbf{s}$ the current element, and $\mathbf{R}$ the vector from the current element to position $\mathbf{r}$. μ is the permeability of the sample and has a value of $4\pi \times 10^{-7} N/A^2$ in free space.

Consider a pair of current loop with current of I and $-I$, centered at $(0,0,z_0)$ and $(0,0,-z_0)$, with radii of r_0, as shown in Figure 4-1, it is easy to show that,

$$\mathbf{r}' = r_0(\cos\varphi'\hat{x} + \sin\varphi'\hat{y}), \tag{4.2}$$

$$d\mathbf{s} = d\mathbf{r}' = r_0 d\varphi'(-\sin\varphi'\hat{x} + \cos\varphi'\hat{y}), \tag{4.3}$$

$$\mathbf{R} = (r\cos\phi - r_0\cos\varphi')\hat{x} + (r\sin\phi - r_0\sin\varphi')\hat{y} + (z - z_0)\hat{z}, \tag{4.4}$$

$$d\mathbf{s} \times \mathbf{R} = r_0 d\varphi'\{(z - z_0)(\cos\varphi'\hat{x} + \sin\varphi'\hat{y}) + [r_0 - r\cos(\varphi' - \phi)]\hat{z}\}. \tag{4.5}$$

Notice that only the $\hat{z}$ component is of interest here, and due to the cylindrical symmetry, it is only necessary to consider the case of $\phi = 0$, thus, the $\hat{z}$ field from

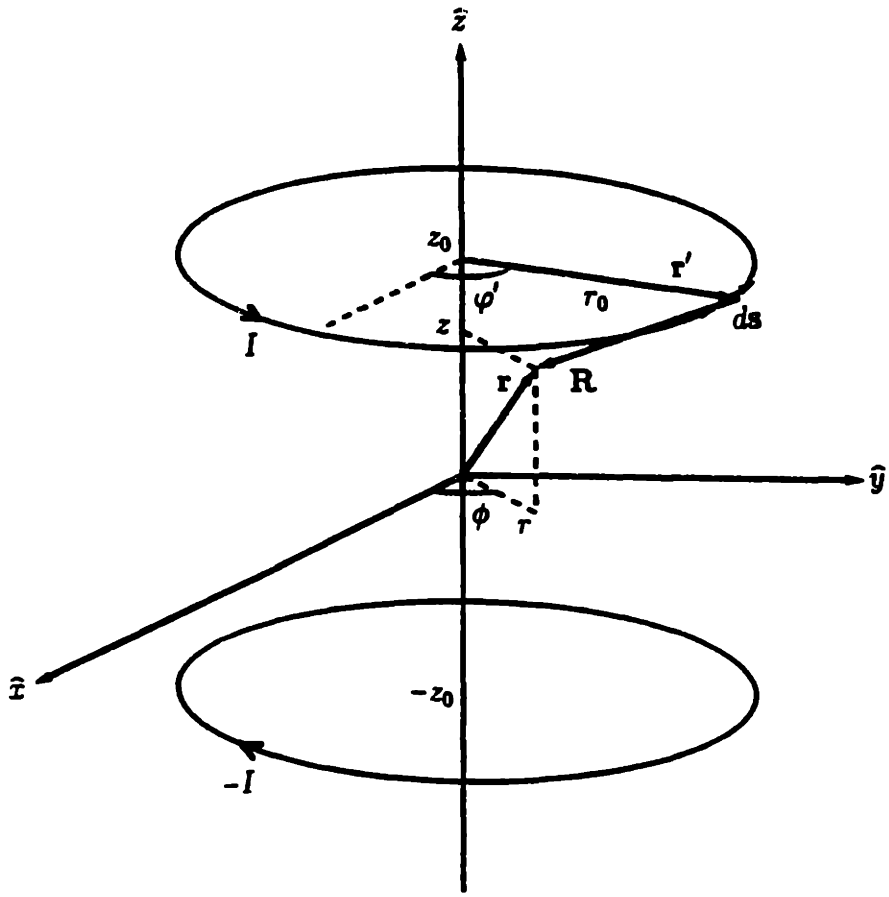

Figure 4-1: An illustration of a Maxwell pair of current loops.

loop 1, centered at $(0, 0, z_0)$, and with a current of I, is,

$$B_z^1(r,z) = \frac{\mu I r_0}{4\pi} \int_0^{2\pi} \frac{(r_0 - r\cos\varphi')d\varphi'}{[r^2 + r_0^2 - 2rr_0\cos\varphi' + (z_0 - z)^2]^{3/2}}. \tag{4.6}$$

Now, include the $\hat{z}$ field due to loop 2, centered at $(0, 0, -z_0)$, and with a current of $-I$, the total $\hat{z}$ field becomes,

$$\begin{aligned} B_z(r,z) &= \frac{\mu I r_0}{4\pi} \int_0^{2\pi} d\varphi'(r_0 - r\cos\varphi') \cdot \left\{ \frac{1}{[r^2 + r_0^2 - 2rr_0\cos\varphi' + (z_0 - z)^2]^{3/2}} \right. \\ &\quad \left. - \frac{1}{[r^2 + r_0^2 - 2rr_0\cos\varphi' + (z_0 + z)^2]^{3/2}} \right\}. \end{aligned} \tag{4.7}$$

Then, the magnetic field gradient along $\hat{z}$ becomes,

$$\frac{\partial B_z(r,z)}{\partial z} = \frac{3\mu I r_0}{4\pi}\int_0^{2\pi} d\varphi'(r_0 - r\cos\varphi')\cdot\left\{\frac{z_0 - z}{[r^2 + r_0^2 - 2rr_0\cos\varphi' + (z_0 - z)^2]^{5/2}} + \frac{z_0 + z}{[r^2 + r_0^2 - 2rr_0\cos\varphi' + (z_0 + z)^2]^{5/2}}\right\}. \quad (4.8)$$

(4.8) can be used to calculate the gradient profile and the gradient coil constant $(T/m/A)$. The gradient at the center of a single turn Maxwell pair is,

$$G_1 = \frac{12\beta\mu I}{(1+\beta^2)^{5/2}D^2}, \quad (4.9)$$

where D is the diameter of the coil and $\beta = 2z_0/D$. For largest volume of useful linear gradients β is chosen to be 0.866 since this geometry eliminates the third order as well as all even order expansion terms in the magnetic field as a function of offset along z [37, 40]. The average coil constant, G_1/I, is inversely proportional to D^2 for a single turn Maxwell pair. At small dimensions, large coil constants are easily obtained, for example, with $\mu \sim 4\pi \times 10^{-7} N/A^2$, if $D = 1mm$, then $G_1/I \approx 3.22T/m/A$, and $300A$ will generate a gradient of $\sim 1000T/m$.

When higher coil constants and better gradient homogeneity are desired, more turns and carefully placed multiple wirings are necessary. Suits and Wilken [40] analyzed the field along the central axis, and found that, for a gradient coil constructed by double blocks of Maxwell pairs, with Z_1, Z_2 defined as the distance of the first and second block from the center, respectively, R defined as the radius of the current loop, and S_2/S_1 defined as the current ratio between the second and the first block, for the conditions $Z_1 = 0.44R$, $Z_2 = 1.19R$, $S_2/S_1 = 7.47$, the third-order, fifth-order, seventh-order and all even order expansion terms in the magnetic field are eliminated.

4.3 The Temperature Increase

The large pulsed currents required for strong gradients lead to coil heating which in addition to raising the temperature of the gradient coil, changes its resistance, and

leads to current decreases when used with a voltage source. The heat dissipation may also raise the temperature and resistance of the nearby RF coil thereby de-tuning the resonance circuit. In the following, a simple calculation of coil heating is employed that assumes there is no heat transfer to the coil form and thus represents a worse case analysis.

In these experiments a voltage source V has been used since it is stable, readily available and inexpensive. The gradient coil is constructed from copper wire with a mass of m_g and a resistance of R_g. Some of the properties of copper at room temperature are: density $\rho \approx 6.4 \times 10^4 kg/m^3$, heat capacity $q_c \approx 4.2 \times 10^2 J/kg \cdot^o C$, resistivity $\rho_r \approx 1.724 \times 10^{-8} \Omega m$, and temperature coefficient of resistivity $\alpha \approx 3.93 \times 10^{-3}/^oC$. If both the on-resistance due to all parts of the circuit other than the gradient coil, R_o, and the coil resistance, R_g, increase with the same factor, then, the temperature changes follow the differential equation,

$$\left\{\frac{V}{(R_o + R_g)[1 + \alpha(T - T_0)]}\right\}^2 R_g[1 + \alpha(T - T_0)]dt = m_g q_c dT, \tag{4.10}$$

which has a solution for the temperature raise from ambient of,

$$\Delta T = \alpha^{-1}\left\{\sqrt{1 + \frac{2\alpha V^2 R_g \Delta t}{(R_o + R_g)^2 m_g q_c}} - 1\right\}, \tag{4.11}$$

where Δt is the total on-time.

For practical coils, $2V^2 R_g \Delta t/(R_o + R_g)^2 m_g q_c << \alpha^{-1} (\approx 254^oC)$, which permits the simplification to,

$$\Delta T \approx \frac{V^2 R_g \Delta t}{(R_o + R_g)^2 m_g q_c}. \tag{4.12}$$

(4.12) describes the temperature increase due to heat dissipation in the coil when the resistance change is not an important contribution. For an n-turn Maxwell pair ($2n$ turns in total) with an average coil diameter D, wire diameter d, $m_g \approx n\pi^2 \rho d^2 D/2$, $R_g \approx 8nD\rho_r/d^2$, and assuming that all resistance arises from the coil,

$$\Delta T \approx (4\pi^2 \rho \rho_r q_c)^{-1} \frac{V^2 \Delta t}{n^2 D^2} \approx 0.055 \frac{V^2 \Delta t}{n^2 D^2}, \tag{4.13}$$

where SI units are used for all variables. To a good approximation, the temperature increase is independent of the wire diameter, but is inversely proportional to n^2 and D^2.

4.4 The Ratio of the Grating Wavenumber to the Coil Temperature Increase

In solid state scattering experiments, large wavenumber gratings are required, however, the coil temperature increases must be limited. It is useful therefore to consider the ratio of the grating wavenumber k ($k = \gamma G \Delta t$, where γ is the gyromagnetic ratio, G is the gradient strength, and Δt is the gradient pulse length.) to the coil temperature increase ΔT as a measure of the coil performance. For the n-turn Maxwell pair geometry, a general result may be derived for this ratio in the case where the gradient scales as the square root of the number of turns

$$\frac{k}{\Delta T} \approx 6\pi^2 \rho q_c \mu \frac{\gamma \beta n^{3/2} d^2}{(1+\beta^2)^{5/2} V D} \approx \frac{2000 \gamma \beta n^{3/2} d^2}{(1+\beta^2)^{5/2} V D}, \tag{4.14}$$

where again SI units are used for all variables. The optimal geometry is then small coils, low source voltages, and large wire diameters with multiple turns. Clearly, there is the additional requirement that a sufficient volume must be provided to contain a detectable number of spins.

4.5 Lorentz Forces and Associated Torques

Regardless of the details of the coil design, pulsed currents of more than $100A$ are delivered in a static magnetic field of $\sim 10T$, resulting in strong Lorentz forces and their associated torques. There is no net force or torque on a current loop that is symmetrically arranged in a magnetic field, however, the current paths that connect to these loops can not all be parallel to the external field and the forces on these must be sustained. In the design illustrated in figure 4-2, the input and return current paths

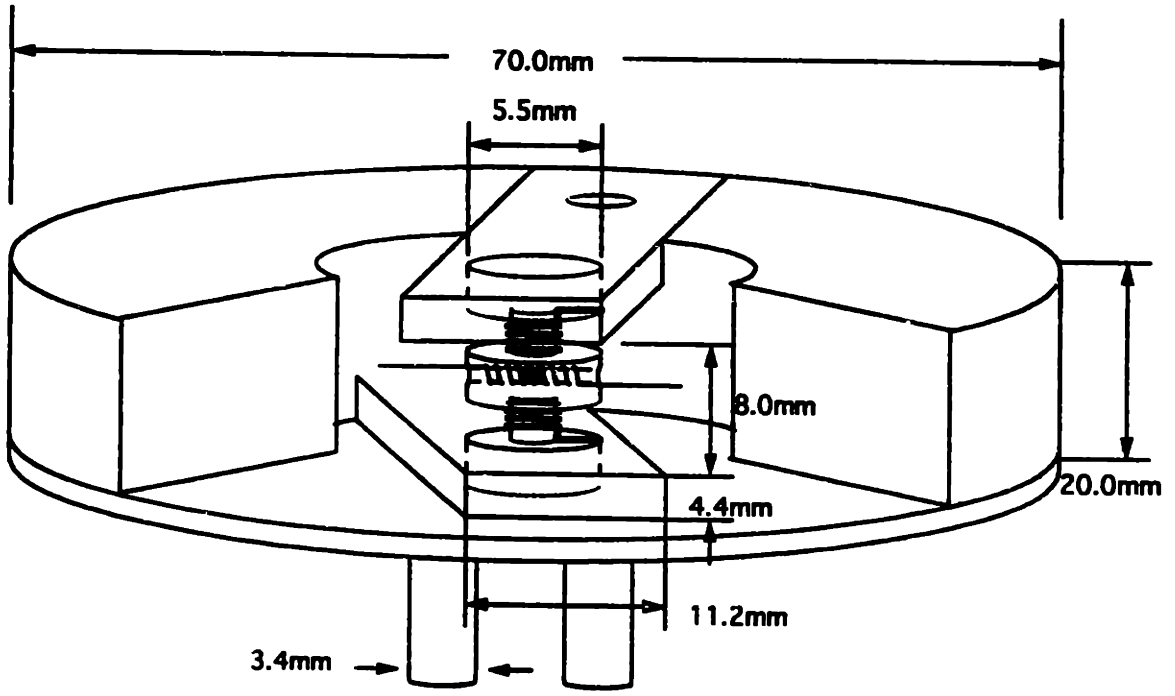

Figure 4-2: A schematic diagram of the gradient set holder. The frame was machined from G-10, and solidly fixed to the probe body. Two copper blocks are fitted into the G-10 frame to support the gradient coil. Currents through the probe is provided by the two copper rods fixed to the copper blocks. The gradient coil is glued to the frame as well as its leads being soldered to the copper blocks.

are each about $2.5cm$ long and are perpendicular to an external field of $\sim 6T$. With a current of $300A$, the Lorentz force is $\sim 45N$. Since the two paths are about 30^0 apart, the net force is $\sim 23N$, and with a distance between the two paths of $\sim 8mm$ the total torque is $\sim 0.35N \cdot m$. As an example, consider a single turn gradient coil constructed from a brass rod, shown in figure 4-3, with an inner diameter of $d_i = 1.4mm$, an outer diameter of $d_o = 5.0mm$, and a length of $l = 8.8mm$, ignoring any asymmetry in this design, the moment of inertia with respect to the center of the cylinder is, $J = \int_{-l/2}^{l/2} z^2 \rho(\pi/4)(d_o^2 - d_i^2)dz = \pi\rho(d_o^2 - d_i^2)l^3/48 \approx 6 \cdot 10^{-8} kg \cdot m^2$. With a torque of $T = 0.35N \cdot m$ acting on its body, the initial angular acceleration would

be $\ddot{\theta} = T/J \approx 7 \cdot 10^6 rad/s^2$ ($\sim 1 cycle/ms^2$) if there wasn't any support!

Any motion of the sample relative to the gradient coil introduces errors in refocusing the spin magnetization grating. A sample size of $500\mu m$ with a grating of $1nm$ requires a precision of $\sim$ 1 in 10^6. Fortunately in solid samples any motions are of the entire sample relative to the gradient set and hence only a phase shift is introduced. So while the sample need not be held to within the pitch of the grating, a robust gradient holder is still necessary and for this work was constructed out of a fiberglass composite, and is illustrated in figure 4-2.

4.6 Three Gradient Sets

For an optimal coil the gradient strength, temperature increase, $k/\Delta T$, Lorentz forces and torques need be considered together. In general, larger numbers of turns improves the performance for all of these factors. Larger wire diameter d and larger coil diameter D increase the ratio of $k/\Delta T$, but they also reduce the gradient coil constant, so some tradeoffs have to be made.

A single turn Maxwell pair gradient coil was designed and machined from a brass rod and cemented to a fiberglass composite for rigidity. The details of the construction are illustrated in figure 4-3. This gradient set has a calibrated average coil constant of $\sim 0.32T/m/A$, a sample diameter of $0.80mm$, and a gradient homogeneity of $\sim \pm 5\%$. Generally, this design has the advantages of a large effective wire diameter, very small resistance, requiring a low source voltage and not suffering much from coil heating. The disadvantages are a low coil constant, relatively poor homogeneity, and the large currents required which introduce large Lorentz forces and torques.

For the measurement of the spin diffusion coefficient in single crystal CaF_2, a 4-turn Maxwell pair gradient coil set was used. The current loops were wound on a coil frame, as shown in Figure 4-4, The calculated gradient profile in the sample region is well confined to $0.68T/m/A \pm 2.0\%$. The average coil constant was calibrated by self-diffusion measurements in water to be $(0.67 \pm 0.02)T/m/A$. This gradient set has both a higher coil constant and a greater homogeneity. The prices paid are a smaller

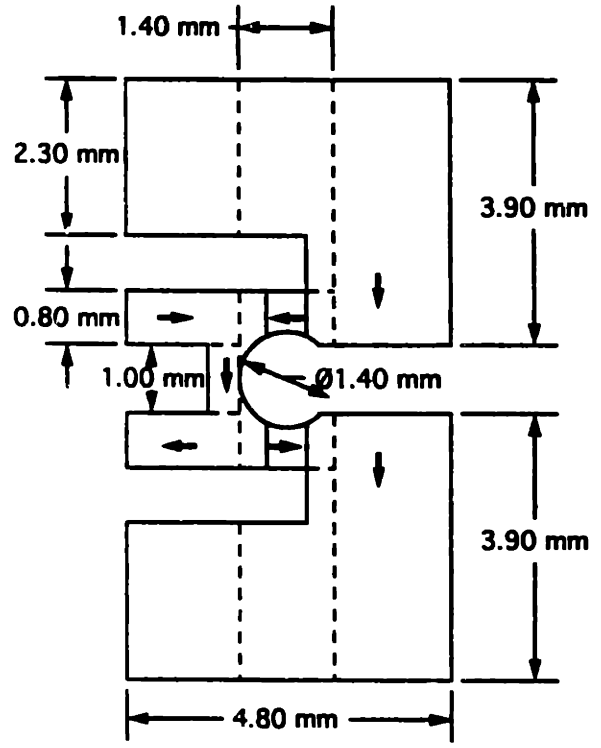

(a)

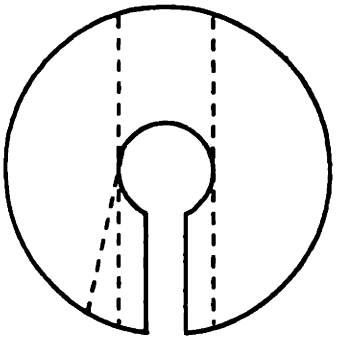

(b)

Figure 4-3: A single-turn Maxwell pair gradient coil machined from a cylindrical brass rod. The average coil constant was calibrated to be $\sim 0.32T/m/A$. AWG34 wires with a diameter of $\sim 0.18mm$ can be used for the RF coil. The sample tube has an outer diameter of $1.00mm$ and an inner diameter of $0.80mm$. (a) Side view of the gradient coil. The arrows show the current directions. The head and the bottom are soldered to the copper blocks shown in Figure 4-2. The central part is the single turn Maxwell pair. (b) Top view of the central Maxwell pair.

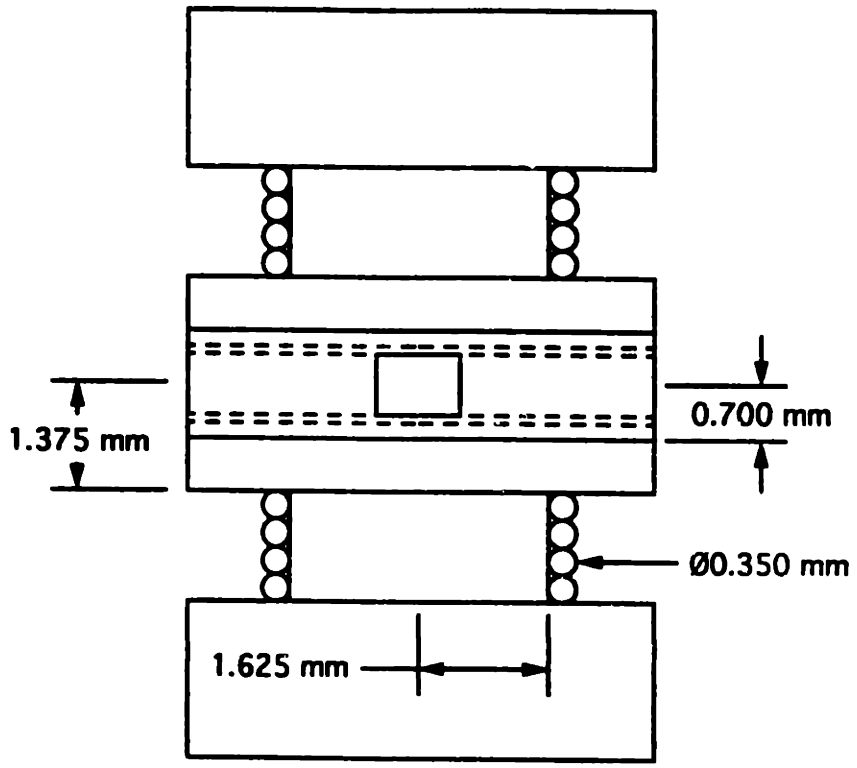

Figure 4-4: A gradient coil set with four turns on each side of the Maxwell pair. The dotted lines denote the sample tube with an outer diameter of $1.00mm$ and an inner diameter of $0.80mm$. AWG28 wires with a diameter of $\sim 0.35mm$ were used for the gradient coil and AWG34 wires with a diameter of $\sim 0.18mm$ were used for the RF coil. The calculated coil constant for a sample region of diameter $0.80mm$ and length $1.00mm$ is $0.68T/m/A \pm 2\%$, and the calibrated average coil constant is $(0.67 \pm 0.02)T/m/A$.

wire diameter, larger resistance and therefore more heat dissipation. Nevertheless, the upper limit of the temperature increase of the gradient coil in the spin diffusion measurement at $k \approx 10\mu m^{-1}$ was less than 2^oC.

Even larger coil constants and better gradient linearity were realized by a third gradient set constructed from two building blocks to approximate the ideal conditions described by Suits and Wilken [40]. Figure 4-5 shows the configuration where 31 turns were wound on each side of the coil frame. The calculated coil constant is $4.01T/m/A$ with a homogeneity of $\pm 0.6\%$. The average coil constant was calibrated again by the

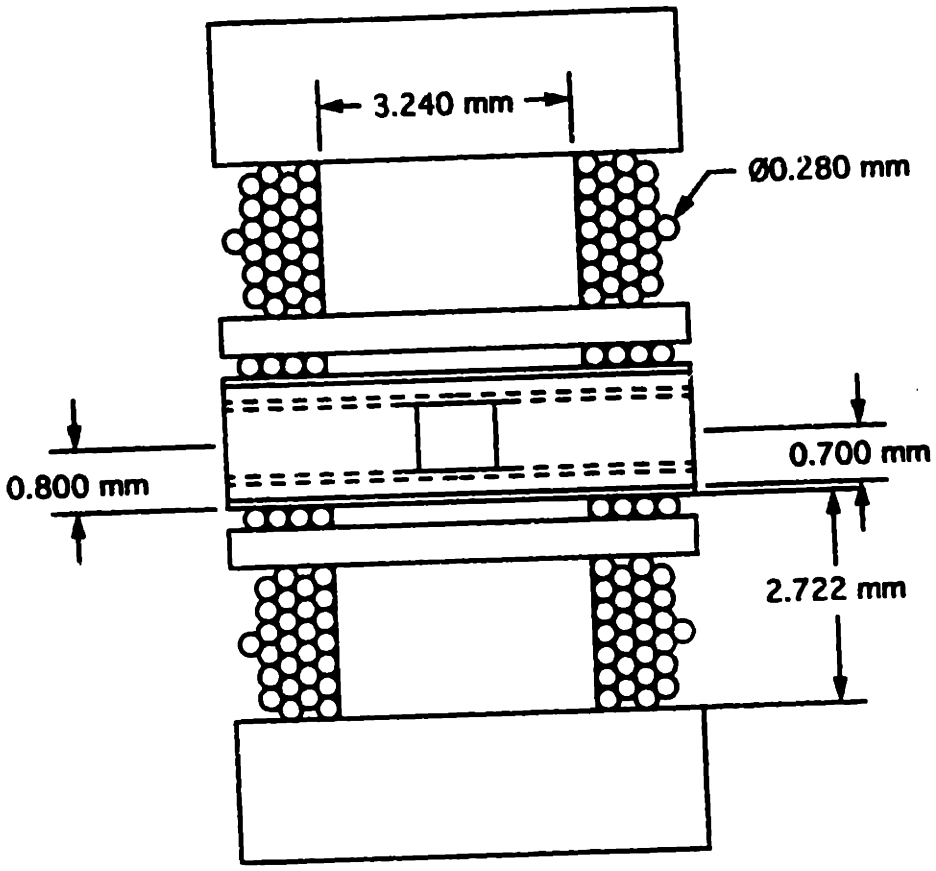

Figure 4-5: A gradient coil set designed for higher coil constant and better gradient profile. The dotted lines denote the sample tube with an outer diameter of $1.00mm$ and an inner diameter of $0.80mm$. AWG30 wires with a diameter of $\sim 0.28mm$ were used for gradient coil while AWG34 wires with a diameter of $\sim 0.18mm$ were used for RF coil. The calculated coil constant for a sample region of diameter $0.80mm$ and length $1.00mm$ is $4.01T/m/A \pm 0.6\%$, and the calibrated average coil constant is $(4.15 \pm 0.04)T/m/A$.

self-diffusion measurements in water and found to be $(4.15 \pm 0.04)T/m/A$. Lower currents are required in this design and thus smaller Lorentz forces and associated torques. Heat dissipation is naturally higher. These three gradient sets are compared in table 4.1.

One of the important experimental issues for scattering experiments is the temperature raise of the gradient coil since this directly effects the gradient calibration. For the 31-turn gradient set, with 30 gauge wire, a total wire length of $0.90m$, $m_g \approx 2.92 \times 10^{-3}kg$ and $R_g \approx 0.31\Omega$, and a voltage source of $48V$ (corresponding

Table 4.1: Compiled features of three gradient sets.

gradient coil set	single turn	4-turn	31-turn
wire resistance	$< 3m\Omega$ (brass)	$20m\Omega$	$310m\Omega$
sample diameter	$0.8mm$	$0.8mm$	$0.8mm$
sample length	$1.0mm$	$1.0mm$	$1.0mm$
coil constant	$0.32T/m/A$	$0.67T/m/A$	$4.15T/m/A$
gradient homogeneity	$\pm 5\%$	$\pm 2\%$	$\pm 0.6\%$
current	$300A$	$300A$	$140A$
Lorentz force	large	large	smaller
gradient strength	$\sim 100T/m$	$\sim 200T/m$	$\sim 600T/m$

to $\sim 140A$), a total current on-time of $\sim 12ms$ is necessary for the creation of a magnetization grating with a pitch of $3nm$ and an upper limit of the temperature increase of $\sim 60°C$ is expected.

In an experiment where 64 current pulses of $200\mu s$ each and a spacing of $400\mu s$ were applied, the measured temperature increase was $\sim 40°C$ and observed gradient coil current dropped from $\sim 140A$ to $\sim 100A$. About half part of this current drop was not due to the coil resistance change but due to the insufficient recovery of the capacitors in the current providing circuit described in the next section.

4.7 A Circuit for Providing Large Pulsed Currents

Conradi et al [41] introduced a circuit to generate short, intense gradient pulses for solid state imaging. The gradient pulses were as short as a few μs, and voltage sources of $\sim 100V$ were used to generate pulsed currents of $\sim 20A$. In this work, the requirement on the gradient pulse length is looser and so, lower voltage sources can be used to generate much larger currents. Figure 4-6 shows the circuit for generating large pulsed currents, using car batteries as the voltage source, and four large storage capacitors (each $4800\mu F$) in parallel to suppress spikes during switching. The bridge circuit is switched by a set of power MOSFETs. FET 1A and 1B provide pulsed currents in one direction, while FET 2A and 2B in the opposite direction. FET 3 and a variable resister R1 provide small pulsed currents for accurate adjustment

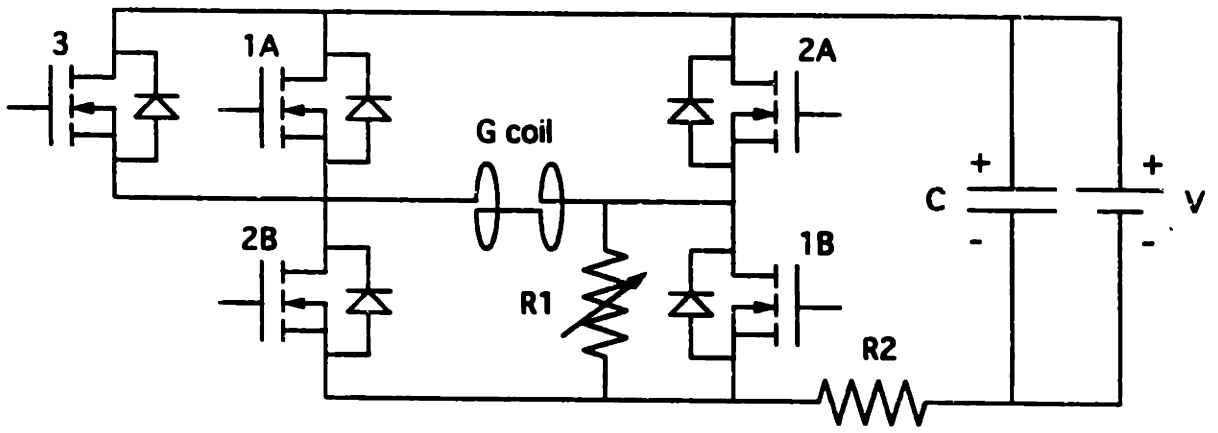

Figure 4-6: The bridge circuit for switching large currents. A voltage source V is used to supply pulsed currents, and large storage capacitors are used to suppress spikes during switching. The bridge circuit is switched by a set of power MOSFETs. FET 1A and 1B provide pulsed currents in one direction, while FET 2A and 2B in the opposite direction. FET 3 and a variable resister R1 provide small pulsed currents for accurate adjustment purposes. A $10m\Omega$ shunt R2 is included in the circuit for accurately calibrating the current amplitudes.

purposes. The power MOSFETs are HARRIS Semiconductor RFA100N05E, each has an on-resistance of $8m\Omega$ and an allowed maximum pulsed current of $300A$. In order to protect from current over-driven, three FETs are used in parallel. Since the switching time of each FET is much faster than the current rising time of the circuit (limited by the large capacitance), the three parallel FETs can be turned on nearly simultaneously, and the on-resonances of the switches are correspondingly decreased by a factor of three. A $10m\Omega$ shunt R2 is included in the circuit for accurately calibrating the current amplitudes, and all other connections, other than the gradient coil, contributed less than $10m\Omega$ resistance.

With a $12V$ car battery, pulsed currents of $\sim 300A$ were delivered to the single turn gradient coil, and currents of more than $200A$ were delivered to the 4-turn gradient coil. With two $12V$ car batteries in serial, currents of $\sim 300A$ were delivered to the

4-turn gradient coil, with four $12V$ car batteries, currents of $\sim 140A$ were delivered to the 31-turn gradient coil. The maximum gradient strengths, achieved with these three gradient sets are $100T/m$, $200T/m$, and $600T/m$.

Chapter 5

Experimental Spin Diffusion Measurement

5.1 NMR Spectrometer Design

An NMR spectrometer was designed and constructed for high resolution NMR scattering experiments. Figure 5-1 shows a schematic diagram. A PTS160 frequency synthesizer is employed to generate a CW RF frequency, which is doubled and then splitted into two channels (called the transmitter channel and the receiver channel). In the transmitter channel, the frequency goes to a 4-phase shifter and a RF switch to get a RF pulse of correct phase. This RF pulse is sent to a power amplifier, followed by a duplexer, with the RF power goes to the probe and the NMR signal goes to the receiver channel. In the receiver channel, the NMR signal passes through a preamplifier and is then mixed down to the audio frequency. These audio signals (real and imaginary) are sampled by two VXI digitizers controlled from a Pentium PC.

The RF switch, power amplifier, 4-phase shifter, digitizers, and gradient bridge circuit discussed in last chapter, need TTL pulses to control. These TTL pulses are generated by a Bruker pulse programmer, which is triggered by one of the two digitizers. The new assignments of TTL pulses for the Bruker pulse programmer are listed in Appendix A, and a sample pulse program is listed in Appendix B. The system control and data transfer are based on VXI buses, and are accomplished by

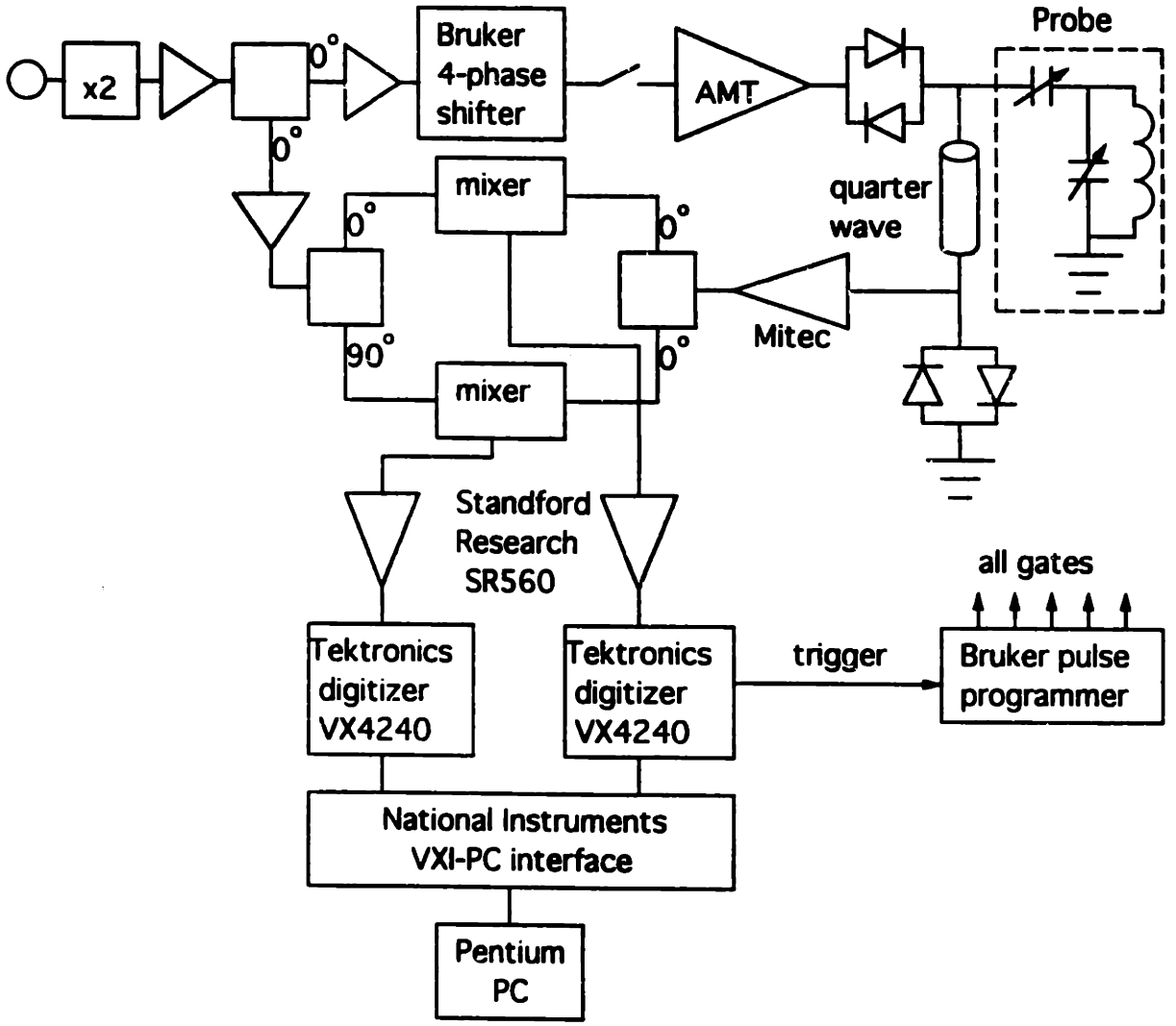

Figure 5-1: A schematic diagram of a home-built NMR spectrometer.

a software package written in C. Appendix C lists a core function to control VXI devices. The experimental data is saved as a binary file and then converted into a Matlab file. Appendix D is the C code for making this conversion. Data processing is done in Matlab.

5.2 The Detailed Pulse Sequence and Experimental Results

In this measurement, a magnetization grating is first created in the nuclear spin system. Spin diffusion attenuates the amplitude of this grating. By monitoring the rate of this attenuation, the spin diffusion coefficient is obtained. The detailed pulse sequence is shown in Figure 5-2. The 90^0 pulse length was $2\mu s$. Some details of the gradient strengths and gradient pulse lengths are provided in Table 5.1. The observed signal is attenuated both by spin diffusion and by spin-lattice relaxation, according to $e^{-t/T_1}e^{-k^2D_{||}t}$, where T_1 is the spin lattice relaxation time, k is the wavenumber of the magnetization grating, and $D_{||}$ is the spin diffusion coefficient for diffusion along the direction of main magnetic field.

The samples for this measurement was a CaF_2 single crystal. Figure 5-3 shows the results of a series of such measurements where the time over which spin diffusion occurred was systematically varied from 10 to 60 seconds for crystal orientations of

Table 5.1: Details of the experimental gradient conditions and resultant gratings that were used for the measurements shown in Figure 5-2.

	pulse length	average current	average strength	$k/2\pi$
[0,0,1] o	100 μs	198.3 A	133 T/m	590 mm^{-1}
[0,0,1] x	90 μs	207.4 A	139 T/m	500 mm^{-1}
[0,0,1] *	70 μs	217.4 A	146 T/m	410 mm^{-1}
[1,1,1] o	200 μs	183.9 A	123 T/m	990 mm^{-1}
[1,1,1] +	180 μs	175.8 A	118 T/m	850 mm^{-1}
[1,1,1] x	140 μs	186.3 A	125 T/m	700 mm^{-1}
[1,1,1] *	110 μs	203.7 A	136 T/m	600 mm^{-1}

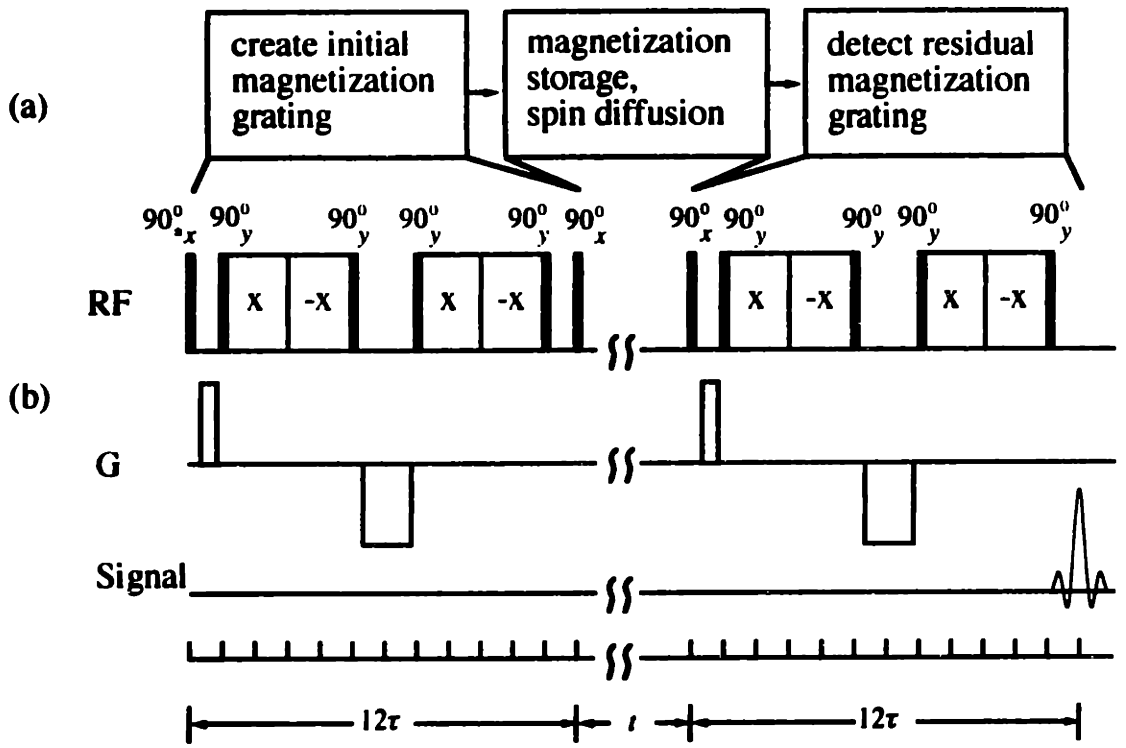

Figure 5-2: Schematic (a) and detailed diagram (b) of the NMR incoherent scattering measurement used to measure the rate of spin diffusion in a homogeneous solid. The method starts by creating a magnetization grating through the otherwise uniform sample. This grating results from the differential rates of spin precession for spins at different spatial offsets in a linear magnetic field gradient. As shown in (b), the time available to create the grating is lengthened by two magic echo cycles which have the added advantage of simultaneously interrupting spin diffusion. During the storage time the z-component of the grating is slowly blurred (or attenuated) by spin diffusion while the transverse components rapidly decay due to the short spin-spin relaxation time. The final period removes the spatial variation in phase so that the extent of attenuation may be measured, and again during this period spin diffusion is interrupted. To measure the spin diffusion constant a series of such experiments were carried out varying both the pitch of the grating and the diffusion (or storage) time.

[0,0,1] and [1,1,1], and the length scales of the magnetization grating were about $1\mu m$ to $3\mu m$. The contribution from the T_1 was measured in a separate set of experiments at these orientations and has been subtracted. These two orientations were chosen since they show the greatest variation in lineshape second moments [19] (see also insert in Figure 5-3). As expected, spin diffusion is Gaussian over this length scale and changes with orientation. The results are compiled in Table 5.2 along with a theoretical prediction of Redfield and Yu from a moment calculation [5] (the value for each orientation was calculated for a 200 × 200 × 200 lattice), Borckmans and Walgraef based on irreversible statistical mechanics [9], and a classical spin dynamic approach of Tang and Waugh [10].

The accuracy of the measured spin diffusion coefficients depends on the calibration of the gradient coil constant, the gradient waveform, an accurate measurement of T_1 and the correct orientation of the crystal. The 4-turn gradient set was used in this measurement. The gradient coil constant was calibrated to the known diffusion constant of water at 15^oC and is $0.67 \pm 0.02T/m/A$. The gradient waveform was directly measured by digitizing the voltage over a shunt to avoid introducing calibration errors for the gradient coil heating. Any errors in gradient calibration are systematic and appear in the absolute diffusion constant, but will not appear in the ratio of the diffusion constants at the two orientations. The T_1 was measured via the same sequence without a magnetization grating. The sample was oriented and cut with the help of X-ray diffraction techniques, but the small ($< 0.8mm$) sized crystals and

Table 5.2: Compiled results of this measurement and previous predictions for single crystal CaF_2. T_1 is the spin-lattice relaxation time, and $D_{||}$ is the component of spin diffusion coefficient parallel to the external magnetic field.

ORIENTATION	[0,0,1]	[1,1,1]
$T_1(s)$(measured)	114.7 ± 5.3	156.8 ± 9.7
$D_{\|\|}(10^{-12}cm^2/s)$(measured)	7.14 ± 0.52	5.31 ± 0.34
$D_{\|\|}(10^{-12}cm^2/s)$([5])	8.22	6.71
$D_{\|\|}(10^{-12}cm^2/s)$([9])	6.98	4.98
$D_{\|\|}(10^{-12}cm^2/s)$([10])	7.42	-

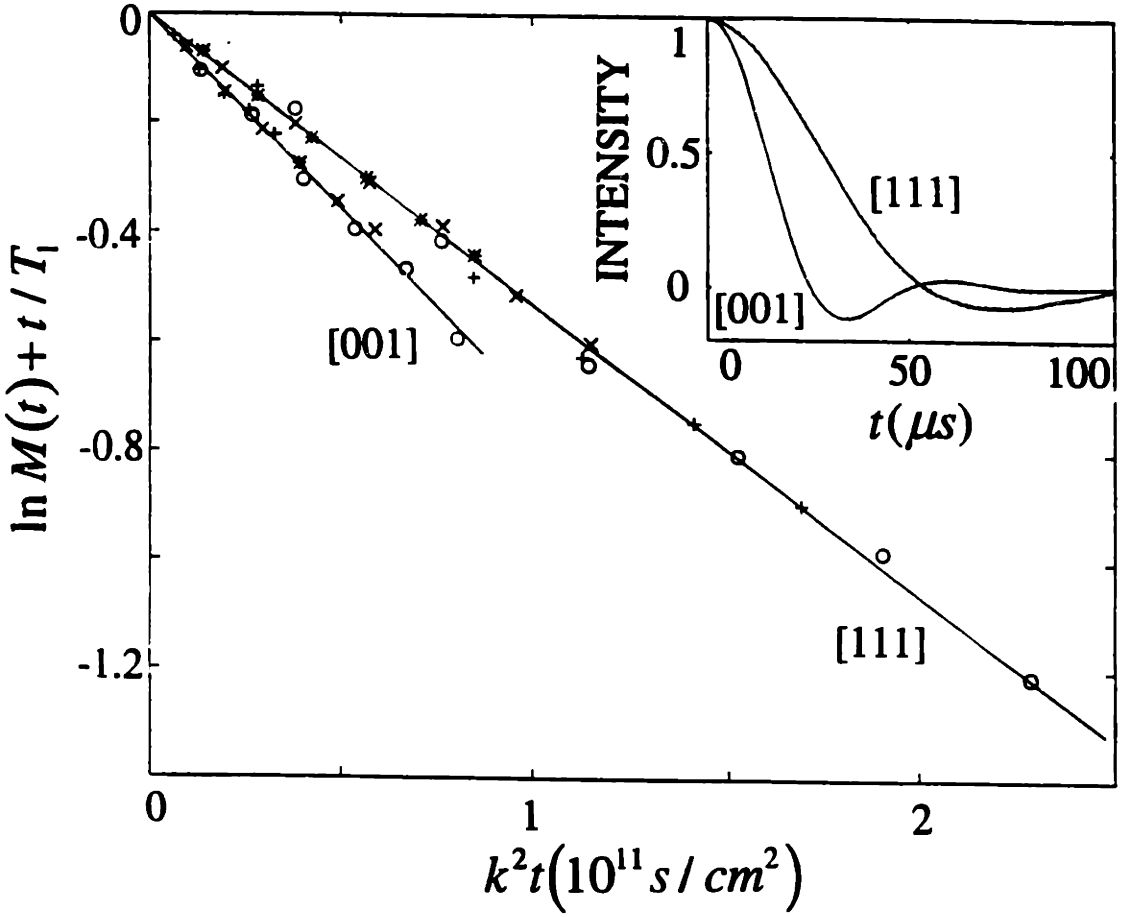

Figure 5-3: Measured signal attenuation from a single crystal CaF_2 oriented with either the [0,0,1] or [1,1,1] axis along the main magnetic field. The contributions to the signal attenuation from relaxation have been subtracted. The diffusion measurements were made with the sequence shown in Figure 5-2, with $\tau = 60\mu s$ for the [0,0,1] orientation and $\tau = 60\mu s$ or $\tau = 100\mu s$ for the [1,1,1] orientation. Both the gradient pulse lengths and the gradient strengths were varied in the experiments, the details are contained in Table 5.1. Notice that for each orientation the data are well described by a straight line, and that the [0,0,1] data decays more rapidly than does the [1,1,1]. The insert shows the measured free induction decay for the two orientations.

limited gradient volume made handling difficult. The measured free induction decays shown as insert in Figure 5-3 are however consistent with those previously reported and so any errors in crystal orientation are small.

The agreement between the measured values and theoretical predictions are quite good, in addition, the ratio of the diffusion constants $D_{||}([0,0,1])/D_{||}([1,1,1]) = 1.3$ which does not suffer from systematic error from gradient coil constant calibration agrees well with the predictions of 1.2 [5] and 1.4 [9].

The spin diffusion rate was also measured for a second crystal with a shorter T_1, therefore containing more defects, oriented along the [1,1,1] direction. As expected, the measured $D_{||}$ is not a function of the defect density. In these scattering measurements the defects introduce spectral mismatches in the surrounding spins and hence locally suppresses the spin diffusion rate. The flow of magnetization which attenuates the grating therefore naturally goes around the defect and exclude it from the dynamics. Provided that the defect density is sufficiently low, the effective tortuosity so introduced does not measurably increase the diffusion constant.

Chapter 6

Conclusion and Future Studies of High Resolution NMR Scattering

In conclusion, the first direct measurement of spin diffusion rate in a homogeneous solid, single crystal CaF_2, has been carried out, and the absolute value and orientation dependence agree well with theoretical predictions. The experiment is an example of an incoherent NMR scattering measurement with a strong pulsed magnetic field gradient probe employed to both create and detect a necessarily fine magnetization grating, and multiple pulse coherent averaging employed to both lengthen the time during which a grating may be established and interrupt spin diffusion during the creation of the grating.

This work can be extended to develop new NMR methods that accurately measure the local distribution of internuclear distances between selected spins over length scales of 5 to 250 $\AA$, and to permit the study of spin dynamics over this same spatial range. Key to achieving these goals is the newly developed strong pulsed magnetic field gradient techniques described in Chapter 4 (with gradient strengths up to $10^3 T/m$, a factor of 100 stronger than those commercially available, and a factor of 25 stronger than the highest previously reported). These gradients can be used to create a Larmor precession frequency that increases linearly with distance at a rate of 50 Hz/nm for ^{1}H.

The essence of the new methods is that by using this gradient, a measurable phase

difference can be developed between dipolarly coupled spins. This phase difference can be made observable in a coherent scattering experiment, or employed with multiple-pulse methods to spatially truncate a network of dipolarly coupled spins. Since the dipolar couplings between spins are appreciable out to only a few hundred angstroms, the creation of gradients strong enough to spatially modulate the spin states over these short distances was a prerequisite for the new studies.

The significance of the new methods will allow chemically selected internuclear distances to be accurately measured on a length scale of 5 to 250 $\AA$, the information being presented as a probability of finding two coupled spins separated by a given distance along the direction of increasing field. The scattering direction can be systematically varied to explore anisotropic materials.

Detailed structural information is not readily available at these length scales particularly for protons, and the experiment can be performed so as to measure the distribution of internuclear proton distances for all protons, between chemically selected protons, or between protons and hetero-atoms. In biomedicine and chemistry such measurements might be aimed at characterizing the local structure of solids, in materials science they could be used to explore the details of interfaces. Used in this fashion, the new methods are complementary to neutron scattering though operating at larger length scale and over longer time intervals.

The spin diffusion rate has been accurately measured (for the first time) in a well defined spin system. The full range of applications will only become known as the method is perfected. The detailed local dynamics of spin transport can also be probed. Note that the measurement should be accurate to a few $\AA$, be chemically selective, and be very local (the sample need only have a coherence length on the scale of the measurement). This will be an ideal approach to studies of mesoscopic scale spin dynamics.

There is a complementary set of experiments that utilize the same instrumentation to truncate spin coupling Hamiltonians along the direction of the gradient (for instance to move between a 3-D and 2-D or 1-D set of coupled spins). Such measurements are very nearly a quantum "simulation" of a quantum system since the effective

Hamiltonian is tailored from the true Hamiltonian. For instance, by varying the average Hamiltonian (through coherent averaging) it is possible to explore the effects of lattice dilation and symmetry breaking without changing the sample. Related methods and the same instrumentation may also be used to implement a form of cellular autonoma that is complementary to the ensemble quantum computing initiative.

The introduction of these new methods, which is collectively termed as *high resolution NMR scattering*, will fundamentally change both the way spin dynamics are studied by NMR and the way spin dynamics are viewed. These methods give the experimentalist, for the first time, a handle on the length scale of spin magnetization transport in strongly coupled systems, and permits spatial degrees of freedom to be included directly in coherent averaging schemes. The potential of this second point includes the preparation of average Hamiltonians in which the residual dipolar coupling is periodically suppressed along the gradient axis and with a spacing that may be tuned to match a specific lattice spacing.

Chapter 7

Measurement of Flow Velocities by NMR using a Spatially Modulated RF Field

7.1 Introduction

NMR methods have long been employed to quantitatively measure flow rates, and generally these methods require a precise control of gradient fields, and an extensive data acquisition and processing step [28]. A typical experiment involves the creation of a magnetization grating, a period during which the grating is allowed to be translated by the flow field, and the detection of the extent of translation. The detection step may be accomplished by refocusing the grating and recording the residual phase shift. Here, we discuss a direct approach to measuring the detailed characteristics of a flow field, where phase encoding in a magnetic field gradient is replaced with a grating geometrically created through a spatially varying RF field, and refocusing is replaced by a frequency readout of the velocity at which the grating flows through the RF coil. A preliminary version of this work has been reported [42], and Goldman and coworkers have discussed a related phenomenon seen when spinning a sample in a quadrupolar RF field [43].

A schematic representation for the experiment is shown in Figure 7-1. As seen in the figure, the RF field is a periodic function whose amplitude oscillates along the coil axis. NMR probes with spatially varying RF fields can be designed from a series of lumped element π-circuits resulting in either an amplitude modulation or a phase modulation. The details are described below. In this introduction concentration will be on flow measurements using a probe with an amplitude modulated RF field. There are two necessary consequences of this geometry related to the spin excitation, and to the detection portions of the experiment (the same coil is employed for each): the RF field strength determines both the spatial variation of the strength of the excitation pulse, and the spatial variation of the spins' coupling to the receiver.

A single excitation pulse will result in a spatial modulation of the spin magnetization along the coil axis. Prior to the experiment the spins are at equilibrium with a net magnetization oriented along the $\hat{z}$ axis. Since the magnitude of the RF field varies with displacement along the coil, then the nutation angle of the excitation pulse reflects this variation, and a magnetization grating is imposed across the sample. Notice that the periodicity of the grating is directly tied to the construction of the RF coil, unlike gratings created by evolution in a magnetic field gradient where the period depends on both the strength of the gradient and the evolution time. The length of the RF pulse only varies the depth of the magnetization grating (assuming that the RF pulse is short with respect to the displacement time).

Naturally, if the spins did not change locations then the NMR signal would not display any spatial information, but as the two gratings move past each other there is (in this case) an amplitude modulation of the NMR signal,

$$S(t) = S_0(t)cos(kvt), \tag{7.1}$$

where $S_0(t)$ is the signal in the absence of motion, k is the wavenumber of the RF field grating, and v is the velocity of the flow.

The Fourier transformation of equation (7.1) is the convolution of the velocity

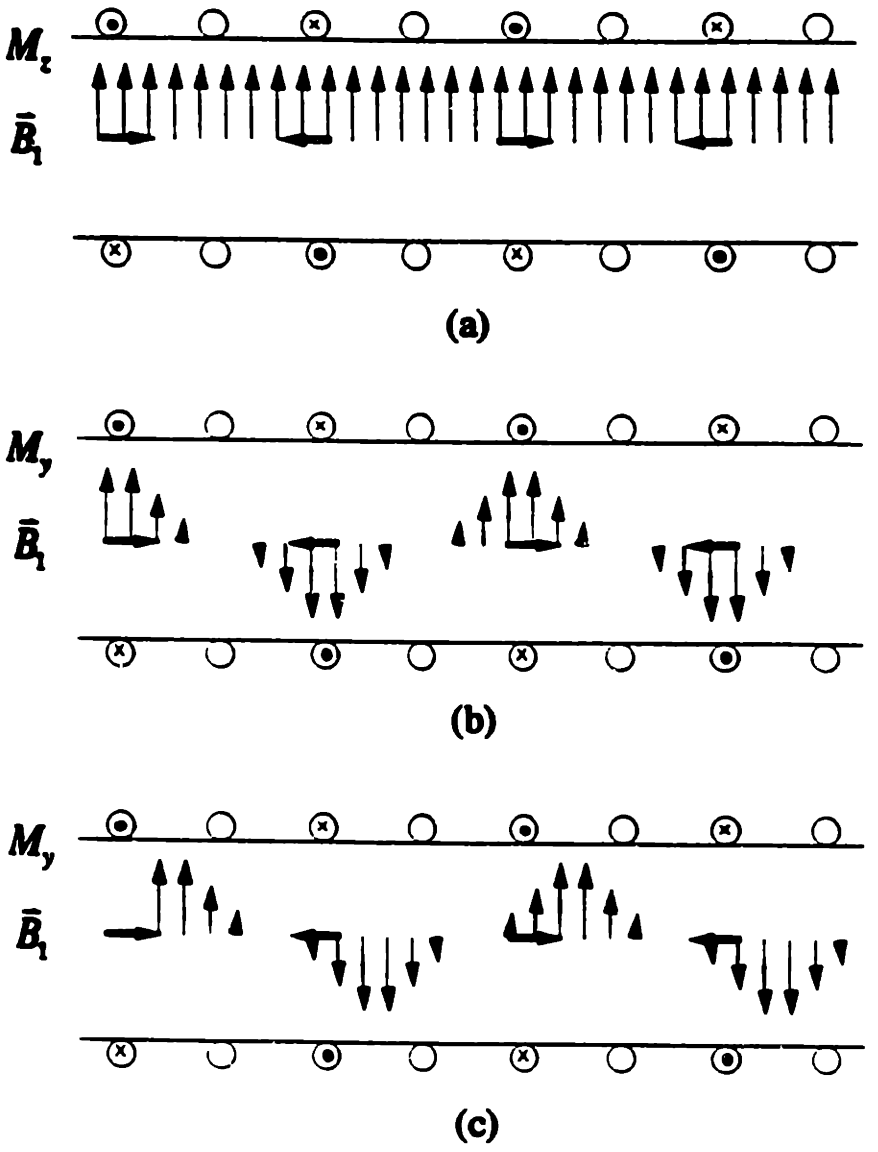

Figure 7-1: An illustration of the flow velocity measurement as made via the NMR response of moving spins excited and detected via a spatially varying RF field. The RF coil windings are displayed schematically for the central slice of the cylindrical coil, along with the instantaneous current directions (dot corresponds to currents out of the page, crosses to currents into the page and blank to no currents). The corresponding RF field is displayed as horizontal vectors of alternating polarity, clearly displaying the amplitude modulation of the field. Superimposed on the diagram are the spin magnetization vectors. In part (a), prior to the excitation pulse the spin magnetization is spatially uniform and oriented along $\hat{z}$. Following the excitation pulse (part (b)) the y-component of magnetization is shown and naturally it reflects the spatial modulation of the RF field. In part (c), the spins have been displaced uniformly and hence the coupling of the spin magnetization to the detection coil is in turn modulated at a rate determined by the velocity.

spectrum with the normal NMR spectrum,

$$\tilde{S}(\omega) = \tilde{S}_0(\omega) \otimes \frac{\delta(\omega + kv) + \delta(\omega - kv)}{2}. \tag{7.2}$$

The spectrum therefore consists of pair of resonances from which the velocity spectrum may be recovered by measuring the splitting.

In complex flows, the spectrum will display the full complexity of the distribution of flow rates. The measurement is linear, and a profile of the relative contributions of each velocity component is obtained. Additionally, each NMR resonance will report on the flow characteristics of the compound from which that resonance arises, so in mixtures of liquids the flow profile of each component is directly measured in a single acquisition step.

The above analysis provides a simple picture of the expected dynamics of the measurement and served as the motivation for starting the project. The real measurement is performed in a truncated coil that may involve a combination of phase and amplitude modulations and below we explore this in some detail. As expected, the main points and inherent simplicity are preserved.

This approach is properly thought of as a simple transducer, that is straightforward to construct. The price that is paid for experimental simplicity is that each transducer is useful over a limited range of flow rates, and over a finite length since there must be a number of cycles of RF modulation to obtain an accurate measure of the flow velocities. This method may be compared to spin tagging methods [44] but retains the advantage that the velocity modulation is directly observed in a single acquisition.

7.2 Detailed Theory of Flow Measurement in a Spatially Varying RF Field

The essence of the measurement is contained within the spatially dependent coupling of the spin magnetization to the receiver. This coupling is proportional to the flux

density that would be created by a unit current through the coil [45], and the signal is the integral of this across the sample. The induced emf across the detection coil, $\xi(t)$, is,

$$\xi(t) = -\int_{sample} \frac{\partial}{\partial t}\{\mathbf{B}_1 \cdot \mathbf{M}(t)\}dV_s, \tag{7.3}$$

where $\mathbf{B}_1$ is the field created by unit current through the coil, and $\mathbf{M}(t)$ is the transverse magnetization.

Notice that the emf accumulates as the projection of the spin magnetization along the RF field, so, if there is no motion then these are everywhere aligned and the NMR response is out of phase with the excitation pulse (assuming the NMR signal is on resonance). In such case, spatial modulations of $\mathbf{B}_1$ are not observed in the response.

The modulation of the NMR signal is revealed by exploring the spatial variations of the magnetization and RF field. Following a RF pulse the transverse magnetization is,

$$\mathbf{M}(\mathbf{r},t) = M(\mathbf{r},t)\{\cos[\omega_0 t + \phi(\mathbf{r})]\hat{x} + \sin[\omega_0 t + \phi(\mathbf{r})]\hat{y}\}, \tag{7.4}$$

where $M(\mathbf{r},t)$ is the amplitude of the transverse magnetization, $\phi(\mathbf{r})$ is its initial phase angle, and ω_0 is Larmor frequency.

Similarly, the RF field is,

$$\mathbf{B}_1(\mathbf{r}) = B_1(\mathbf{r})[\cos\varphi(\mathbf{r})\hat{x} + \sin\varphi(\mathbf{r})\hat{y}], \tag{7.5}$$

where $B_1(\mathbf{r})$ is the amplitude of the field, and $\varphi(\mathbf{r})$ is the phase angle of the field.

The core of the integral of equation (7.3) then becomes,

$$-\frac{\partial}{\partial t}\{\mathbf{B}_1 \cdot \mathbf{M}(t)\} = B_1(\mathbf{r})M(\mathbf{r},t)\omega_0 \sin[\omega_0 t + \phi(\mathbf{r}) - \varphi(\mathbf{r})]. \tag{7.6}$$

Transforming this into the rotating frame where $\Delta\omega = \omega_0 - \omega$, and neglecting the component oscillating at $\omega_0 + \omega$, yields a general formula for the detected emf in the rotating frame, $\xi_r(t)$,

$$\xi_r(t) = -\frac{i}{2}\omega_0 \int_{sample} B_1(\mathbf{r})M(\mathbf{r},t)e^{i[\Delta\omega + \phi(\mathbf{r}) - \varphi(\mathbf{r})]}dV_s. \tag{7.7}$$

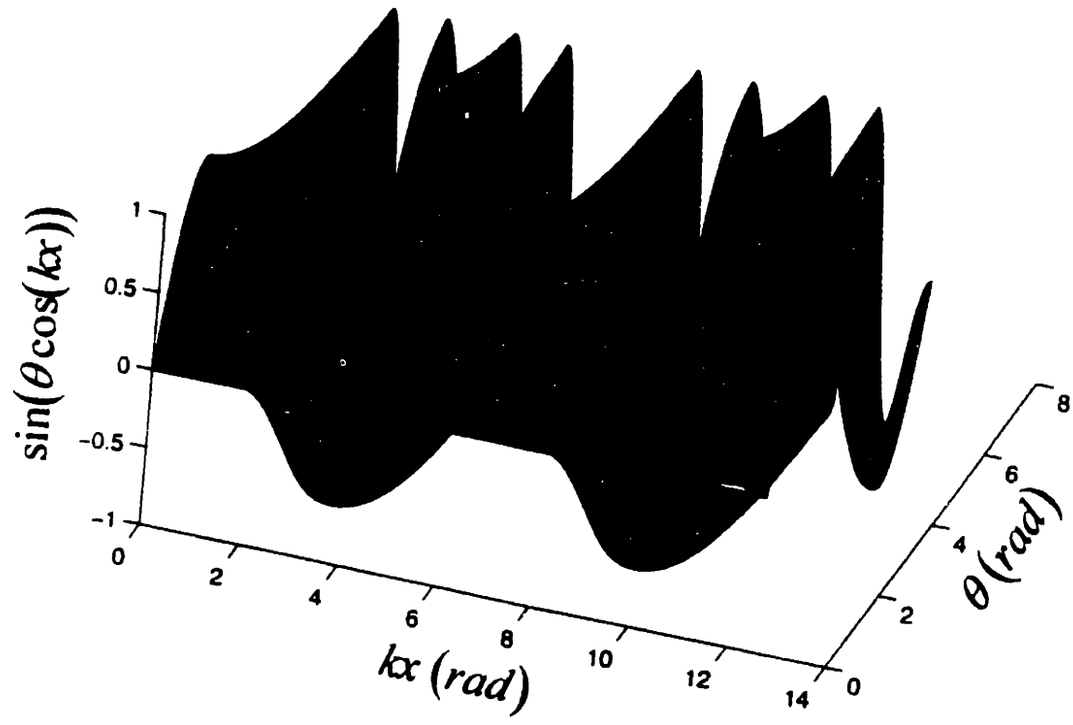

Figure 7-2: An illustration of the $\hat{y}$ magnetization grating following a single nutation pulse as described by (7.9), where the nutation angle θ varies from 0 to 2π, and the spatial phase angle kx varies from 0 to 4π. Notice that for low flip angles the grating is well described by the fundamental, but at higher flip angles spatial harmonics appear.

The NMR signal is the emf integrated over the sample for a particular excitation pulse, and RF profile. Here, the field is assumed to be cosine modulated in amplitude, that is,

$$B_1(x) = \begin{cases} B_1 \cos(kx) & 0 \le x \le L \\ 0 & \text{otherwise} \end{cases}, \varphi(x) = 0, \tag{7.8}$$

where k is the wavenumber of the $\mathbf{B}_1$ field, and L is the coil's length.

With the spin system originally at equilibrium, $\mathbf{M} = M_0\hat{z}$, a RF pulse of length t_p nutates the bulk magnetization into the transverse plane, such that,

$$\mathbf{M}(x, t=0) = \begin{cases} -M_0 \sin[\theta \cos(kx)]\hat{y} + M_0 \cos[\theta \cos(kx)]\hat{z} & 0 \le x \le L \\ M_0\hat{z} & \text{otherwise} \end{cases}, \tag{7.9}$$

where $\theta = \gamma B_1 t_p$, and γ is the gyromagnetic ratio.

Figure 7-2 shows the dependence of the transverse magnetization on nutation angle

θ and spatial phase angle kx, where θ varies from 0 to 2π, and kx varies from 0 to 4π. It is clear that, a spatial magnetization grating has been created in the transverse plane for each specific θ, and the depth of this grating varies with the value of θ, which is especially pronounced for $\theta \leq \pi/2$. In addition to the fundamental spatial frequency with wavenumber k, there are higher harmonics of these. As the amplitude of the nutation pulse increases, the relative contribution of the higher spatial harmonics increase. The intensity of the fundamental is a maximum for $\theta \approx 0.586\pi$. It is the motion of this grating through the periodic RF field that will permit a measure of the flow velocity. It is interesting to note that the harmonics arise directly from the modulation pattern, and so we can expect to see harmonic behavior in the spin dynamics regardless of the length of the RF coil.

Now, concentrating on the transverse magnetization only, and including the translation of spins due to flow, then,

$$M(x,t) = \begin{cases} M_0 \sin\{\theta \cos[k(x-vt)]\} & 0 \leq x - vt \leq L \\ 0 & \text{otherwise} \end{cases}, \phi(x) = -\frac{\pi}{2}, \qquad (7.10)$$

where v is the flow velocity.

From (7.7), then the detected signal in the rotating frame is seen to be,

$$\xi_r(t) = -\frac{1}{2}\omega_0 B_1 M_0 S e^{i\Delta\omega t} \int_{vt}^{L} \cos(kx) \sin\{\theta \cos[k(x-vt)]\} dx, \qquad (7.11)$$

where S is the cross section area of the sample, and the integration is over the volume of the sample within the coil suitably reduced by the flow to account for those spins that leave the coil.

The above description of the detected signal is rather inconvenient, and may be placed into a more recognizable form by expanding the integral in terms of Bessel functions:

$$\xi_r(t) = -\frac{1}{2}\omega_0 B_1 M_0 S e^{i\Delta\omega t} \Big\{ J_1(\theta)(L - vt)\cos(kvt)$$

$$+\sum_{n=0}^{\infty}\frac{(-1)^n J_{2n+1}(\theta)}{2(n+1)k}\{\sin[2(n+1)kL-(2n+1)kvt]-\sin(kvt)\}$$
$$+\sum_{n=1}^{\infty}\frac{(-1)^n J_{2n+1}(\theta)}{2nk}\{\sin[2nkL-(2n+1)kvt]+\sin(kvt)\}\Big\}, \qquad (7.12)$$

where $J_{2n+1}(\theta)$ is the Bessel function of order $(2n+1)$. This predicts that the spectrum has multiple peaks, because the magnetization grating created in this case has harmonics of the fundamental and therefore multiple wave components exist. In the case of small θ the response is well described by a single harmonic and corresponds to a narrow-band FM modulation. For $\theta = 0.586\pi$ and $2\pi/k << L$, the first term dominates and the spectrum is well described by two peaks shifted by $\Delta f = \pm kv/2\pi$ from the normal resonance position. Other terms lead to a series of sidebands at $\Delta f = \pm(2n+1)kv/2\pi$. Only the $n = 0$ term gives an appreciable signal which, however, overlaps with the main peaks.

Since k is the wavenumber of the $\mathbf{B}_1$ field, which is controlled by the RF field design, the flow velocity may be easily and accurately determined simply by measuring the frequency shift in the detected signal. In addition to the flow modulation, there is an extra damping term, $(L - vt)$, which is associated with spins leaking out of the coil, and contributes to the spectrum broadening. The velocity resolution of this simplest form of the experiment is therefore dependent on the length of the coil.

Simpler calculations can be used for a phase modulated RF field, where the signal evolves as e^{ikvt} instead of $\cos(kvt)$. This introduces a frequency shift instead of peak splitting, and is similar to that described by Goldman and coworkers [43].

7.3 Design of Probes with Spatially Varying RF fields

There are many ways to design probes with spatially modulated RF fields. One easy approach is to geometrically arrange the wiring of the coil. A simple example is a quadruple coil which can generate a phase modulated RF field [46]. For a solenoid coil, alternately inverting the current paths of the neighboring turns can create an

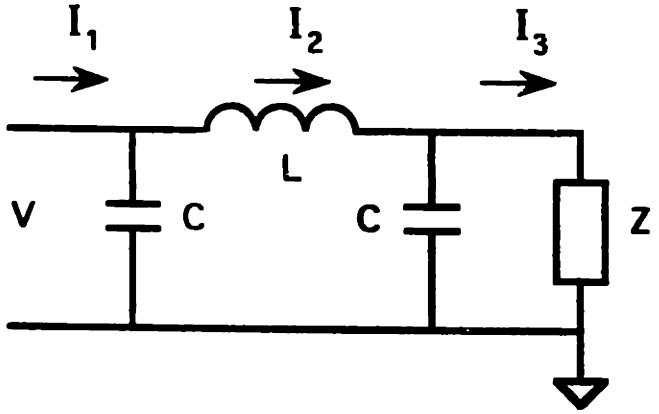

Figure 7-3: A C-L-C π-section where V is the input voltage, I_1, I_2, I_3 are the currents around the circuit, and Z is the load. The input impedance of the circuit is $Z_{in} \equiv V/I_1$.

amplitude modulated RF field.

Here, however, we present a design that employs the transmission properties of a resonant π-circuit. Generally we expect such a design to be more efficient and of higher quality factor than the purely geometric designs. Such a probe can easily be constructed to have either an amplitude or phase modulated RF field.

As reported by Fukushima and Roeder [47], the C-L-C π-section, shown in Figure 7-3, with an input impedance of $Z_{in} \equiv V/I_1$ and a load of Z, obeys the property,

$$Z_{in} \cdot Z = Z_0^2, \text{ for } \omega = 1/\sqrt{LC}, \tag{7.13}$$

so, on resonance, the π-section is identical to a quarter wave line with characteristic impedance of $Z_0 = \sqrt{L/C}$. This circuit also displays the well known quarter wave impedance transformation property that if the load is an ideal inductor, it is transformed into an ideal capacitor at the input, and vice versa.

For the application described here, the current at each point in the circuit is of particular interest since the field throughout the coil is directly tied to this. It can

be shown that, on resonance ($\omega = 1/\sqrt{LC}$),

$$I_2 = (1 - i\frac{Z_0}{Z})I_1, \tag{7.14}$$

$$I_3 = -i\frac{Z_0}{Z}I_1, \tag{7.15}$$

please refer to Figure 7-3 for the definitions of the currents.

Three special cases are useful:

a) if $Z = i\omega L$, then $I_2 = 0$, $I_3 = -I_1$ and $Z_{in} = 1/i\omega C$;

b) if $Z = 1/i\omega C$, then $I_2 = 2I_1$, $I_3 = I_1$ and $Z_{in} = i\omega L$;

c) if $Z = Z_0$, then $I_2 = \sqrt{2}e^{-i\pi/4}I_1$, $I_3 = e^{-i\pi/2}I_1$ and $Z_{in} = Z_0$.

A probe with an amplitude modulated RF field can be built based on the first two cases. The probe consists of an even number of π-sections connected in series as shown in Figure 7-4(a) with an inductor as the load. After an even number of quarter wave impedance transformations, the load is transformed back into an inductor at the input of the π-series, so the matching and tuning circuits are identical to those conventionally used in NMR probes. However, a spatially modulated RF field is created by the alternating current distribution. The period of the RF field and the number of the cycles are tied directly to the geometric construction of the probe.

The same basic scheme can be used to build a probe with a phase modulated RF field by employing case c) above. A simplified scheme is shown in Figure 7-4(b). The characteristic impedance of the resonant π-circuit is designed to be 50Ω. So if the "load circuit" of the π-series is tuned and matched to 50Ω at the resonance frequency, it will be transformed into 50Ω at the input. Now, each π-network acts as a delay line and the current in the two consecutive coils are exactly 90^0 out of phase.

Through an extension of the current transformation by a series of resonant π-networks, RF fields with amplitude modulation, phase modulation, or both, can be created through the choice of load. These designs are certainly not the only choice of circuits, but do have the benefits of simplicity and of maintaining a relatively high self resonance frequency and high quality factor.

This analysis of the current behavior is simplified and intended to show the prin-

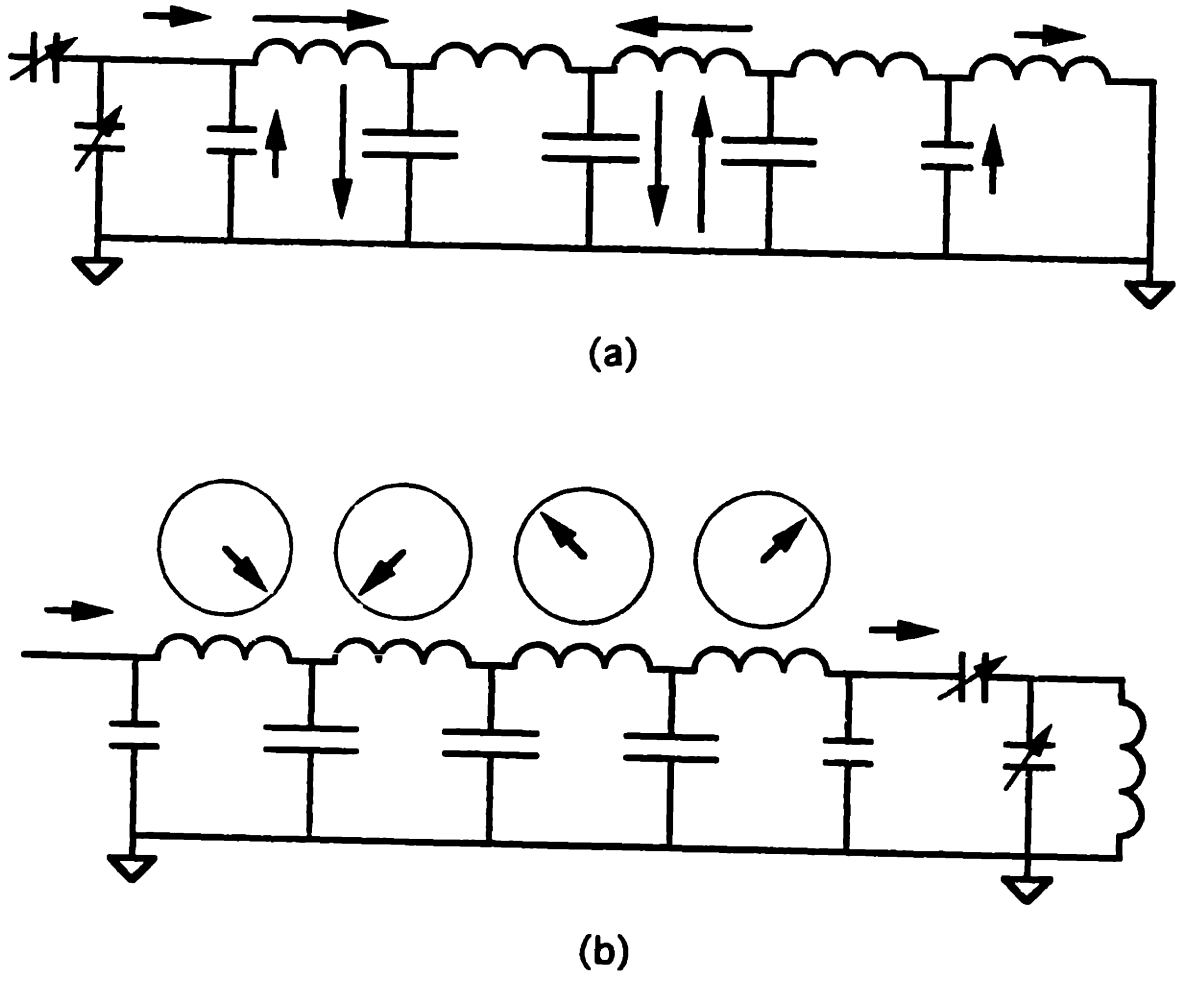

Figure 7-4: Amplitude and phase modulated probe designs. (a) An amplitude modulated probe of four π-sections. The two parallel capacitors in neighboring π-sections were replaced by a single capacitor of twice the capacitance. (b) The corresponding phase modulated probe of four π-sections. The phase of the current in the coil of each π-section is shown in the complex plane. The currents in two consecutive coils are exactly 90^0 out of phase.

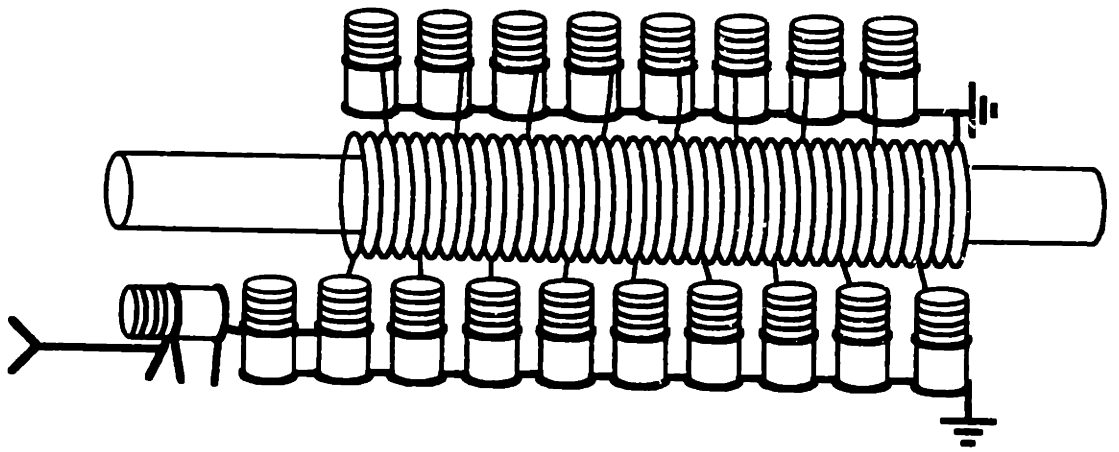

Figure 7-5: The geometry of an NMR probe designed for flow measurement experiment. The construction follows the circuit shown in Figure 7-4(a), with 16 cascaded quarter wave π-sections. The coil diameter is $9.5mm$, and in each section, the coil has 3 turns. The total coil length for the 16 cascaded π-sections is $4.7cm$. An additional 3-turn coil is connected at the end of the last section, so that the total coil length for the entire probe is $5.0cm$. The first π-section is connected to tuning and matching capacitors, and the two capacitors between every two coils were replaced by a single variable capacitor. These capacitors were tuned with the help of a network analyzer and a small movable pickup coil. Direct measurement from the network analyzer confirms the design of an amplitude modulated RF field.

ciple of how the amplitude or phase of the current may be made spatially varying. In practice, each inductor has an associated resistance which must be included in the analysis along with any mutual inductances.

The particular probe used for studies reported here was designed to have an amplitude modulated $\mathbf{B}_1$ field. The construction is shown in Figure 7-5 and the details is described in the figure caption.

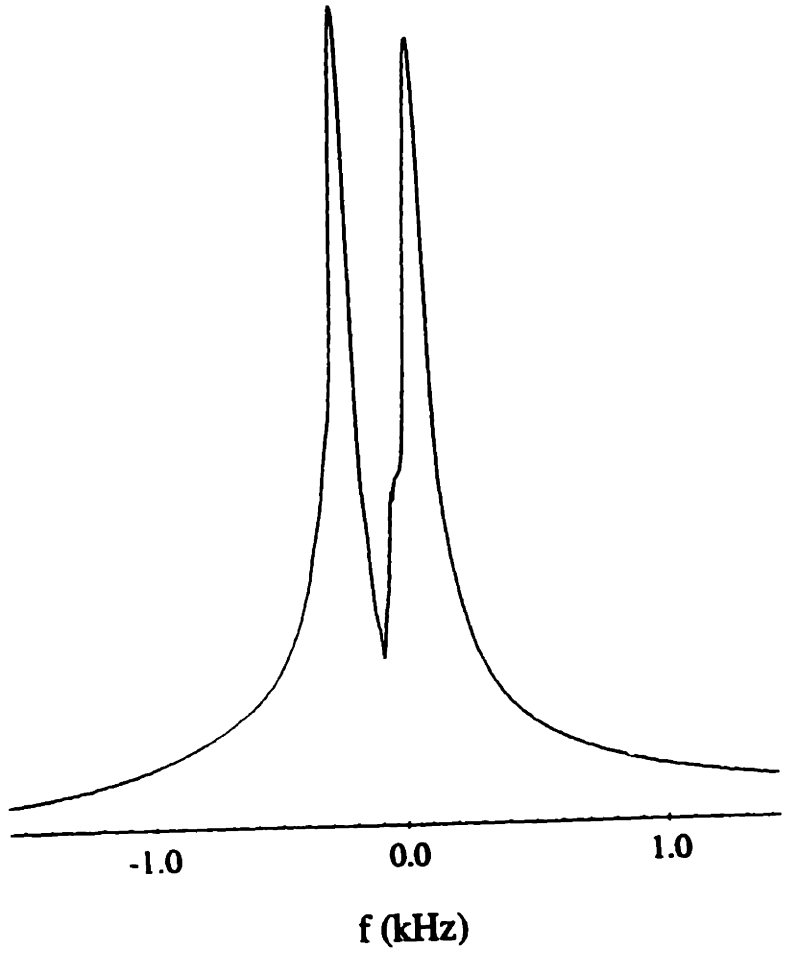

Figure 7-6: A typical frequency spectrum for the amplitude modulated signal detected in the presence of flow. Notice the peaks' splitting and broadening.

7.4 Experimental Results

The experiments were performed on a $4.7T$ magnet with a home-built console. Water flowed through the coil under a simple gravity feed with the flow rates varied. Under these conditions, a few tens of centimeters of tubing was sufficient for T_1 relaxation of the spins prior to entering the coil. Flow rates of from $\sim 10cm/s$ to $\sim 220cm/s$ (as roughly measured by the fill rate of a calibrated cylinder) were explored. The experimental results agree with theoretical predictions, the central peak for the stationary sample is split into two peaks in the presence of flow, and the frequency shifts are proportional to the flow velocities.

Figure 7-6 shows a typical spectrum for the detected signal in the presence of flow.

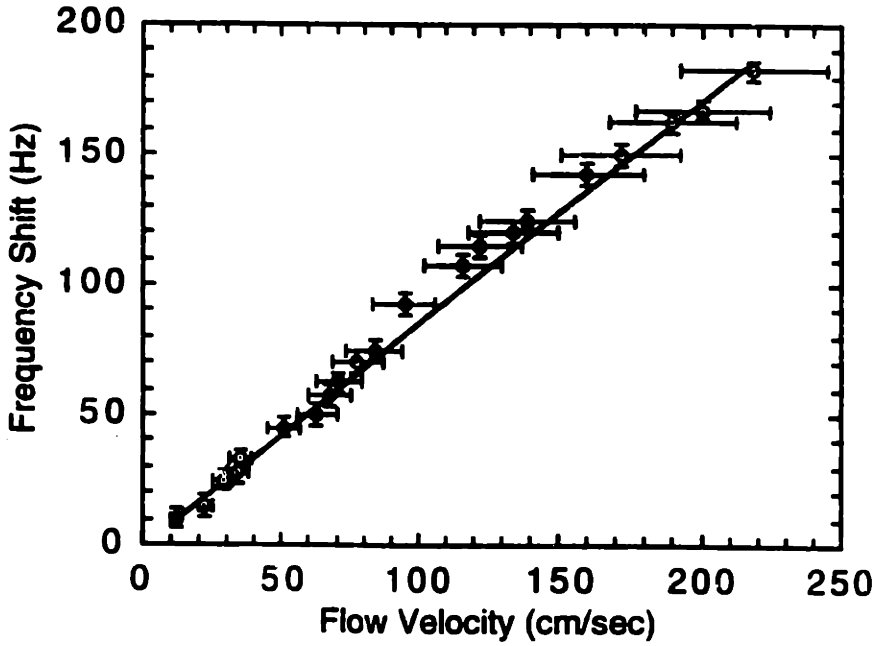

Figure 7-7: The measured frequency shift vs. flow velocity. The data was fit by linear regression, and the slope indicates a measured k of $1.75\pi/cm$, in good agreement with the designed value of $1.70\pi/cm$.

Notice the spectral broadening, which has three contributions, the $(L - vt)$ leakage term in equation (7.12), the distribution of flow velocities, and the T_2^* relaxation. For these measurements, the field inhomogeneity term is quite pronounced since susceptibility matched wire was not used and the variable capacitors were placed directly on the coil.

Figure 7-7 shows the measured frequency shifts at different flow velocities. It is clear that the frequency shift is proportional to the flow velocity. A small systematic error in the non-NMR measurements of the flow accounts for the deviation from linearity. A value of k of $1.75\pi/cm$ was measured both with a small pickup coil and from a fit of the frequency shift. This agrees quite well with the designed value of $1.70\pi/cm$.

7.5 Extensions for Measuring Slow Flows

There is a built-in lower limit to the flow velocity that can be measured by the described one pulse approach, and higher k probes must be employed. However, very high k probes are not easily constructed, and the associated fields fall off rapidly with distance from the surface of the coil. A much simpler approach to the measurement of slow flows is to make use of the residual magnetization along the $\hat{z}$ direction. A two pulse sequence which is analogous to a stimulated echo can then be used to measure flows via a time of flight sequence. After the excitation pulse, the magnetization in the transverse plane is spatially modulated. Only this magnetization is used in the one pulse experiment. However, from (7.9), it is seen that the residual magnetization along $\hat{z}$ is also spatially modulated after the pulse. The transverse magnetization decays quickly due to T_2^* relaxation. But the spatial modulation in the $\hat{z}$ magnetization remains for a time comparable to T_1. This $\hat{z}$ magnetization grating translates slowly along $\hat{x}$. A second pulse (or a series of small tip angle pulses) can be employed to monitor the progress of the spins through the coil, which can in turn be used to accurately calibrate the velocity of the translating spins. Naturally, the maximum signal occurs when the $\hat{z}$ magnetization grating overlaps exactly with the $\mathbf{B}_1$ field grating.

Appendix A

Hardware Specifications

Table A.1: Voltage supply assignments for the home-built NMR spectrometer.

Voltage	Supply From	Supply To
+19V	Bruker Console Back Panel 1 (A)	Transmitter/Receiver Box
Ground	Bruker Console Back Panel 1 (CC)	Transmitter/Receiver Box
-19V	Bruker Console Back Panel 1 (P)	Transmitter/Receiver Box
+19V	Bruker Console Back Panel 1 (E)	4-Channel Phase Shifter Box
Ground	Bruker Console Back Panel 1 (HH)	4-Channel Phase Shifter Box
-19V	Bruker Console Back Panel 1 (K)	4-Channel Phase Shifter Box
+19V	Bruker Console Frequency Unit RFT (k)	40dB Preamplifier Box
Ground	Bruker Console Frequency Unit RFT (HH)	40dB Preamplifier Box

Table A.2: The new assignments of TTL pulses for the Bruker pulse programmer.

Function	Channel	Pin in ACQ P2
External Trigger In (From VX4240 Digitizer S3-8)		B
RF Pulse Gate	f1	D
Phase Shifter Control TTL0	C2	T
Phase Shifter Control TTL1	C3	R
RF Unblanking	C4	P
Receiver Gate (Reserved)	C5	M
Digitizer Sampling Trigger	C6	L
Gradient Control 1	C7	X
Gradient Control 2	C8	V
Gradient Control 3	C9	S
Reserved	C10	N
Reserved	C11	K
Reserved	C12	F
Reserved	f2	E
Reserved	f3	R

Appendix B

A Sample Pulse Program

```
;;;;;;;;;;;;;;;;;;;;;;;;;;;; Solid Echo Sequence ;;;;;;;;;;;;;;;;;;;;;;;;;;;;
100u ;;;;; delay 100 microseconds
trigp ;;;;; wait for positive TTL level
2u ;;;;; delay 2 microseconds
trign ;;;;; wait for negative TTL level
;;;;;;;; The pulse programmer will wait until
;;;;;;;; the Acquisition Processor P2(B) detects a trigger
;;;;;;;; armed by digitizer B (see also Appendix C).
;;;;;;;; The following is the "real" solid echo pulse sequence.
(4u p1 4u):f1 p2:C4 ;;;;; 90 degree x pulse. p2=4us+p1+4us
d1 ;;;;; delay d1.
(4u p1 4u):f1 (4u p1 4u):C2 p10:C4 ;;;;; 90 degree y pulse.
10u ;;;;; delay 10 microseconds
p3:C6 ;;;;; Sampling trigger. p3 can be chosen as 2us or other values.
d2 ;;;;; delay d1.
```

Appendix C

A Core Function to Control VXI Devices

```
/*****************************************************************/
/****************************** wsexmp.c *****************************/
/****************** A core function to control VXI devices ***************/
/*****************************************************************/
#include "stdio.h"
#include "string.h"
#include "nivxi.h"
#include "ws.h"
#include "main.h"
UINT8 *write_buff = (UINT8 *) "LADDRS?"; /* buffer to write in WSwrt */

void wsexmp (void)
{
INT16 la,retval;
UINT16 comm,respflag,response,mode;
UINT32 count, retcount;
INT32 timeout, actualtimo;
UINT8 read_buff[200];
INT8 *filename;
char *yes;
int i;

/**** The following code sets the timeout period to 10 seconds ****/
timeout = 10000L;
retval = WSsetTmo(timeout,&actualtimo);

/*****************************************************************/
/******** Sampling parameters are sent to digitizer A, logical address 20 ********/
/*****************************************************************/
```

```
la = 20;
mode = WSb_MODE_NO_DirDorAbort | WSb_MODE_SendEnd ;

/**** Reset VX4240 digitizer ****/
write_buff= "R\n"; /* Reset Command */
count = (UINT32)strlen(write_buff);
retval = WSwrt(la,write_buff,count,mode,&retcount);

/**** Set digitizer to be DC coupling, +-2.0 volt, 50 ohm, single ended input ****/
write_buff= "VD2FS\n";
count = (UINT32)strlen(write_buff);
retval = WSwrt(la,write_buff,count,mode,&retcount);

/**** Set digitizer sampling dwell time to be 0.1 microsecond, internal clock ****/
write_buff= "P0.1E-6\n";
count = (UINT32)strlen(write_buff);
retval = WSwrt(la,write_buff,count,mode,&retcount);

/**** Set digitizer to collect 4 records of 2500 samples (10000 samples total) ****/
write_buff= "CR2500/4\n";
count = (UINT32)strlen(write_buff);
retval = WSwrt(la,write_buff,count,mode,&retcount);

/**** Set digitizer to delay 3 sample after the trigger ****/
write_buff= "DS3\n";
count = (UINT32)strlen(write_buff);
retval = WSwrt(la,write_buff,count,mode,&retcount);

/**** Set digitizer to be external sampling triggered: negative TTL edge ****/
write_buff= "ME-\n";
```

```
count = (UINT32)strlen(write_buff);
retval = WSwrt(la,write_buff,count,mode,&retcount);

/**** Arm the trigger ****/
write_buff= "TA\n";
count = (UINT32)strlen(write_buff);
retval = WSwrt(la,write_buff,count,mode,&retcount);

/*************************************************************************/
/******** Sampling parameters are sent to digitizer B, logical address 25 ********/
/*************************************************************************/

la = 25;
mode = WSb_MODE_NO_DirDorAbort | WSb_MODE_SendEnd ;

/**** Reset VX4240 digitizer ****/
write_buff= "R\n"; /* Reset Command */
count = (UINT32)strlen(write_buff);
retval = WSwrt(la,write_buff,count,mode,&retcount);

/**** Set digitizer to be DC coupling, +-2.0 volt, 50 ohm, single ended input ****/
write_buff= "VD2FS\n";
count = (UINT32)strlen(write_buff);
retval = WSwrt(la,write_buff,count,mode,&retcount);

/**** Set digitizer sampling dwell time to be 0.1 microsecond, internal clock ****/
write_buff= "P0.1E-6\n";
count = (UINT32)strlen(write_buff);
retval = WSwrt(la,write_buff,count,mode,&retcount);
```

```
/**** Set digitizer to collect 4 records of 2500 samples (10000 samples total) ****/
write_buff= "CR2500/4\n";
count = (UINT32)strlen(write_buff);
retval = WSwrt(la,write_buff,count,mode,&retcount);

/**** Set digitizer to delay 3 sample after the trigger ****/
write_buff= "DS3\n";
count = (UINT32)strlen(write_buff);
retval = WSwrt(la,write_buff,count,mode,&retcount);

/**** Set digitizer to be external sampling triggered: negative TTL edge ****/
write_buff= "ME-\n";
count = (UINT32)strlen(write_buff);
retval = WSwrt(la,write_buff,count,mode,&retcount);

/**** Arm the trigger. Trigger the pulse programmer (see also Appendix B) ****/
write_buff= "TA\n";
count = (UINT32)strlen(write_buff);
retval = WSwrt(la,write_buff,count,mode,&retcount);

/*************************************************************************/
/**************** Data transfer from digitizer A, logical address 20 ************/
/*************************************************************************/

la = 20;
count = 8;

/**** check the status of the digitizer until the sampling is completed ****/
do {
retval = WSrd(la,read_buff,count,mode,&retcount);
```

```
} while (read_buff[5]=='0');

/**** Set the input request: incremental, offset:0 ****/
write_buff= "II0TS1\n";
count = (UINT32)strlen(write_buff);
retval = WSwrt(la,write_buff,count,mode,&retcount);

/**** The following code reads from VX4240 and write to file "vx4240a.dat" ****/
filename="vx4240a.dat";
count = 20000L; /* 10000 data points, 20000 bytes */
mode = WSb_MODE_NO_DirDorAbort | WSb_MODE_NoEndEnd;
retval = WSrdf(la,filename,count,mode,&retcount);

/*************************************************************************/
/*************** Data transfer from digitizer B, logical address 25 ***********/
/*************************************************************************/

la = 25;
count = 8;

/**** check the status of the digitizer until the sampling is completed ****/
do {
retval = WSrd(la,read_buff,count,mode,&retcount);
} while (read_buff[5]=='0');

/**** Set the input request: incremental, offset:0 ****/
write_buff= "II0TS1\n";
count = (UINT32)strlen(write_buff);
retval = WSwrt(la,write_buff,count,mode,&retcount);
```

```
/**** The following code reads from VX4240 and write to file "vx4240b.dat" ****/
filename="vx4240b.dat";
count = 20000L; /* 10000 data points, 20000 bytes */
mode = WSb_MODE_NO_DirDorAbort | WSb_MODE_NoEndEnd;
retval = WSrdf(la,filename,count,mode,&retcount);

}
```

Appendix D

A C Code for Converting Binary Data Files into Matlab Data Files

```
/*****************************************************************/
/****************************** b2m.c ********************************/
/******** This program convert binary data files into Matlab data files ********/
/*****************************************************************/
#include "stdio.h"
#include "math.h"
main()
{
struct header
{
long type; /* when using PC and DEC RISC, type=0 */
long nrows; /* # of rows */
long ncols; /* # of cols */
long imagf; /* imagf=0: data real, imagf=1: data imag */
long namelen; /* length of matrix name + 1 */
/* the matrix is referred (or used) in matlab */
};
struct header x1;
FILE *outfile,*infile;
int i,j;
double out_img[1][500];
char *pname;
unsigned char in_img[1000];

/**** Convert binary data file "vx4240a.dat" into "vx4240a.mat" ****/
infile=fopen("vx4240a.dat","rb");
x1.type=0;
x1.nrows=1;
x1.ncols=10000;
x1.imagf=0;
```

```
x1.namelen=8;
pname= "vx4240a"; /* matrix name is "vx4240a" */
outfile=fopen("vx4240a.mat","w");
fwrite(&x1,sizeof(x1),1,outfile); /* write out header info. */
fwrite(pname,sizeof(char),x1.namelen,outfile); /* write out matrix name */
for (i=0;i<20;i++)
fread(in_img,sizeof(unsigned char),1000,infile);
for (j=0;j<500;j++)
out_img[0][j]= (double)(((in_img[2*j])<<8)+in_img[(2*j+1)]);
fwrite(out_img[0], sizeof(double), 1*500,outfile); /* write out matrix */
}
fclose(infile);
fclose(outfile);

/**** Convert binary data file "vx4240b.dat" into "vx4240b.mat" ****/
infile=fopen("vx4240b.dat","rb");
x1.type=0;
x1.nrows=1;
x1.ncols=10000;
x1.imagf=0;
x1.namelen=8;
pname= "vx4240b"; /* matrix name is "vx4240b" */
outfile=fopen("vx4240b.mat","w");
fwrite(&x1,sizeof(x1),1,outfile); /* write out header info. */
fwrite(pname,sizeof(char),x1.namelen,outfile); /* write out matrix name */
for (i=0;i<20;i++)
fread(in_img,sizeof(unsigned char),1000,infile);
for (j=0;j<500;j++)
out_img[0][j]= (double)(((in_img[2*j])<<8)+in_img[(2*j+1)]);
fwrite(out_img[0], sizeof(double), 1*500,outfile); /* write out matrix */
```

```
}
fclose(infile);
fclose(outfile);

}
```

Bibliography

[1] N. Bloembergen. On the Interaction of Nuclear Spins in a Crystalline Lattice. *Physica*, 15:386, 1949.

[2] E. R. Andrew, K. M. Swanson, and B. R. Williams. Angular Dependence of Nuclear Spin-Lattice Relaxation Time for Several Alkali Halide Crystals. *Proceedings of the Physical Society*, 77:36, 1961.

[3] G. W. Leppelmeier and J. Jeener. Measurement of the Nuclear Spin Diffusion Coefficient in CaF_2. *Physical Review*, 175:498, 1968.

[4] A. G. Redfield. Spatial Diffusion of Spin Energy. *Physical Review*, 116:315, 1959.

[5] A. G. Redfield and W. N. Yu. Moment Method Calculation of Magnetization and Interspin-Energy Diffusion. *Physical Review*, 169:443, 1968.

[6] A. G. Redfield and W. N. Yu. Erratum: Moment Method Calculation of Magnetization and Interspin-Energy Diffusion. *Physical Review*, 177:1018, 1969.

[7] I. J. Lowe and S. Gade. Density-Matrix Derivation of the Spin-Diffusion Equation. *Physical Review*, 156:817, 1967.

[8] I. J. Lowe and S. Gade. Erratum. Density-Matrix Derivation of the Spin-Diffusion Equation. *Physical Review*, 166:934, 1968.

[9] P. Borckmans and D. Walgraef. Irreversibility in Paramagnetic Spin Systems: Free Induction Decay and Spin Diffusion. *Physical Review*, 167:282, 1968.

[10] C. Tang and J. S. Waugh. Dynamics of Classical Spins on a Lattice: Spin Diffusion. *Physical Review B*, 45:748, 1992.

[11] W.-K. Rhim, A. Pines, and J. S. Waugh. Time-Reversal Experiments in Dipolar-Coupled Spin System. *Physical Review B*, 3:684, 1971.

[12] S. Zhang, B. H. Meier, and R. R. Ernst. Polarization Echoes in NMR. *Physical Review Letters*, 69:2149, 1992.

[13] H. M. Pastawski, P. R. Levstein, and G. Usaj. Quantum Dynamical Echoes in the Spin Diffusion in Mesoscopic Systems. *Physical Review Letters*, 75:4310, 1995.

[14] E. Fischer, R. Kimmich, and N. Fatkullin. Spin Diffusion in Melts of Entangled Polymers. *Journal of Chemical Physics*, 106:9883, 1997.

[15] D. G. Cory. Solid State NMR Imaging. *Annual Report on NMR Spectroscopy*, 24:87, 1992.

[16] D. G. Cory, J. B. Miller, R. Turner, and A. N. Garroway. Multiple-Pulse Methods of ^{1}H N.M.R. Imaging of Solids: Second-Averaging. *Molecular Physics*, 70:331, 1990.

[17] K. Takegoshi and C. A. McDowell. A "Magic Echo" Pulse Sequence For The High-Resolution NMR Spectra of Abundant Spins in Solids. *Chemical Physics Letter*, 116:100, 1985.

[18] S. Matsui. Solid-State NMR Imaging by Magic Sandwich Echoes. *Chemical Physics Letter*, 179:187, 1991.

[19] A. Abragam. *Principles of Nuclear Magnetism.* Clarendon, 1961.

[20] J. H. Van Vleck. The Dipolar Broadening of Magnetic Resonance Lines in Crystals. *Physical Review*, 74:1168, 1948.

[21] T. Morita. Spin Diffusion in the Heisenberg Magnets at Infinite Temperature. *Physical Review B*, 6:3385, 1972.

[22] M. Goldman and L. Shen. Spin-spin Relaxation in LaF_3. *Physical Review*, 144:321, 1966.

[23] P. Caravatti, P. Neuenschwander, and R. R. Ernst. Characterization of Heterogeneous Polymer Blends by Two-Dimensional Proton Spin Diffusion Spectroscopy. *Macromolecules*, 18:119, 1985.

[24] J. R. Havens and D. L. VanderHart. Morphology of Poly(ethlene terephthalate) Fibers as Studied by Multiple-Pulse ^{1}H NMR. *Macromolecules*, 18:1663, 1985.

[25] R. Brüschweiler and R. R. Ernst. A Cog-Wheel Model for Nuclear-Spin Propagation in Solids. *Journal of Magnetic Resonance*, 124:122, 1997.

[26] W. E. Blumberg. Nuclear Spin-Lattice Relaxation Caused by Paramagnetic Impurities. *Physical Review*, 119:79, 1960.

[27] P. L. Kuhns, P. C. Hammel, O. Gonen, and J. S. Waugh. Unexpectedly rapid ^{19}F Spin-Lattice Relaxation in CaF_2 Below 1K. *Physical Review B*, 35:4591, 1987.

[28] P. T. Callaghan. *Principles of Nuclear Magnetic Resonance Microscopy*. Clarendon, 1991.

[29] A. Z. Genack and A. G. Redfield. Theory of Nuclear Spin Diffusion in a Spatially Varying Magnetic Field. *Physical Review B*, 12:78, 1975.

[30] A. G. Genack. Dipole Energy Dissipation and Nuclear Spin Diffusion in Mixed-State Superconducting Vanadium. *Physical Review B*, 13:68, 1976.

[31] A. A. Samoilenko, D. Yu. Artemov, and L. A. Silbel'dina. Formation of Sensitive Layer in Experiments on NMR Imaging of Solids. *JETP Letters*, 47:417, 1988.

[32] R. Kimmich, W. Unrath, G. Schnur, and E. Rommel. NMR Measurement of Small Self-Diffusion Coefficients in the Fringe Field of Superconducting Magnets. *Journal of Magnetic Resonance*, 91:136, 1991.

[33] O. Züger, S. T. Hoen, C. S. Yannoni, and D. Rugar. Three-Dimentional Imaging with a Nuclear Magnetic Resonance Force Microscopy. *Journal of Applied Physics*, 79:1881, 1996.

[34] A. Schaff and W. Veeman. Mechanically Detected Nuclear Magnetic Resonance at Room Temperature and Normal Pressure. *Journal of Magnetic Resonance*, 126:200, 1997.

[35] M. S. Crawford, B. C. Gerstein, A.-L. Kuo, and C. G. Wade. Diffusion in Rigid Bilayer Membranes. Use of Combined Multiple Pulse and Multiple Pulse Gradient Techniques in Nuclear Magnetic Resonance. *Journal of the American Chemical Society*, 102:3728, 1980.

[36] E. O. Stejskal and J. E. Tanner. Spin Diffusion Measurements: Spin Echoes in the Presence of a Time-Dependent Field Gradient. *Journal of Chemical Physics*, 42:288, 1965.

[37] J. E. Tanner. Pulsed Field Gradients for NMR Spin-Echo Diffusion Measurements. *The Review of Scientific Instruments*, 36:1086, 1965.

[38] R. F. Karlicek, Jr., and I. J. Lowe. A Modified Pulsed Gradient Technique for Measuring Diffusion in the Presence of Large Background Gradients. *Journal of Magnetic Resonance*, 37:75, 1980.

[39] S. Choi, X.-W. Tang, and D. G. Cory. Constant Time Imaging Approaches to NMR Microscopy. *International Journal of Imaging System Technology*, 8:263, 1997.

[40] B. H. Suits and D. E. Wilken. Improving Magnetic Field Gradient Coils for NMR Imaging. *Journal of Physics E: Scientific Instruments*, 22:565, 1989.

[41] M. Conradi, A. N. Garroway, D. G. Cory, and J. B. Miller. Generation of Short, Intense Gradient Pulses. *Journal of Magnetic Resonance*, 94:370, 1991.

[42] W. Zhang and D. G. Cory. The Direct Measure of Flow Rates via RF Gradients. Presentation at the 36th Experimental Nuclear Magnetic Resonance Conference, 1995, Boston.

[43] M. Goldman, V. Fleury, and M. Guëron. NMR Frequency Shift under Sample Spinning. *Journal of Magnetic Resonance*, 118:11, 1996.

[44] J. R. Singer. Blood Flow Rates by NMR Measurements. *Science*, 130:1652, 1959.

[45] D. I. Hoult and R. E. Richard. The Signal-to-Noise Ratio of the Nuclear Magnetic Resonance Experiment. *Journal of Magnetic Resonance*, 24:71, 1976.

[46] D. G. Cory, F. H. Laukien, and W. E. Mass. NMR Spectroscopy with Radial Pulses. P- and N-Type Selection COSY. *Chemical Physics Letters*, 212:487, 1993.

[47] E. Fukushima. *Experimental Pulse NMR: A Nuts and Bolts Approach.* Addison-Wesley, 1981.